

# Transient Tropopause Waves

ANDREAS DÖRNBRACK<sup>a</sup>

<sup>a</sup> *Deutsches Zentrum für Luft- und Raumfahrt, Institut für Physik der Atmosphäre, Oberpfaffenhofen, Germany*

(Manuscript received 8 March 2024, in final form 10 June 2024, accepted 8 July 2024)

**ABSTRACT:** Flight-level airborne observations have often detected gravity waves with horizontal wavelengths  $\lambda_x \lesssim 10$  km near the tropopause. Here, in situ and remote sensing aircraft data of these short gravity waves trapped along tropopause inversion layer and collected during a mountain-wave event over southern Scandinavia are analyzed to quantify their spectral energy and energy fluxes and to identify nonstationary modes. A series of three-dimensional numerical simulations are performed to explain the origin of these transient wave modes and to investigate the parameters on which they depend. It turns out that mountain-wave breaking in the middle atmosphere and the subsequent modification of the stratospheric flow are the key factors for the occurrence of trapped modes with  $\lambda_x \lesssim 10$  km. In particular, the intermittent and periodic breaking of mountain waves in the lower stratosphere forms a wave duct directly above the tropopause, in which the short gravity waves are trapped. The characteristics of the trapped, downstream-propagating waves are mainly controlled by the sharpness of the tropopause inversion layer. It could be demonstrated that different settings for optimizing the numerical solver have a significantly smaller influence on the solutions.

**KEYWORDS:** Gravity waves; Wave breaking; Tropopause; Middle atmosphere

## 1. Introduction

Short gravity waves with horizontal wavelengths  $\lambda_x \lesssim 10$  km were frequently observed during research flights near the tropopause (e.g., Smith et al. 2008; Woods and Smith 2010; Zhang et al. 2015; Wagner et al. 2017; Smith and Kruse 2017; Witschas et al. 2017; Gisinger et al. 2020).


Previous airborne observations during T-REX (Grubišić et al. 2008) and Deep Propagating Gravity Wave Experiment (DEEPWAVE) (Fritts et al. 2016) found that  $\lambda_x$  is limited by a lower cutoff wavelength  $\lambda_c \approx 2\pi U/N$ , with estimates of wind speed  $U$  and buoyancy frequency  $N$  taken from characteristic tropospheric or stratospheric values. In many cases, the wave phases could not be associated with orographic features of the underlying terrain (e.g., Woods and Smith 2010). Instead, the occurrence of the short waves near the tropopause was interpreted as indirect evidence for the excitation of secondary waves in the middle atmosphere and their subsequent downward propagation. These conclusions were based on idealized 2D and 3D numerical simulations (Woods and Smith 2011).

Here, and as, for example, in Satomura and Sato (1999) and Woods and Smith (2011), secondary waves are understood as internal gravity waves generated by nonlinear processes in a vertically propagating finite-amplitude mountain wave excited by flow over the terrain (see, e.g., Vadas and Fritts 2001; Vadas et al. 2003, for an explanation of the general mechanism of secondary wave generation). Recent 3D nonlinear studies specifically address the generation of secondary gravity waves in the middle atmosphere (e.g., Fritts

et al. 2020; Dong et al. 2022). These studies simulated the interaction of given wave packets with thermal and/or Doppler ducts (Isler et al. 1997). Wave ducts, sometimes called waveguides, are atmospheric layers in which the squared vertical wavenumber  $m^2$  ( $m = 2\pi/\lambda_z$ ,  $\lambda_z$  is the vertical wavelength) is positive, but the regions below and above have negative  $m^2$  values.

As suggested by Woods and Smith (2010), the observations of T-REX revealed that the gravity waves with  $\lambda_x \lesssim 10$  km can be trapped along the tropopause inversion layer (TIL; see Birner et al. 2002, for a definition and climatological analysis). Besides the mentioned upper atmosphere ducts (e.g., Isler et al. 1997; Snively and Pasko 2008; Suzuki et al. 2010; Dong et al. 2022), there exist tropospheric as well as stratospheric wave ducts (Danielsen and Bleck 1970). Well-known examples are mountain lee waves (e.g., Wurtele et al. 1996). A vivid example of a nearly monochromatic secondary gravity wave with  $\lambda_x \lesssim 10$  km capping a polar stratospheric cloud below a wave-breaking region was visualized by combining airborne lidar observation and high-resolution numerical simulations (Dörnbrack et al. 2002, Fig. 5). This wave appears to be trapped in the midstratosphere.

The T-REX results were based on the curious finding that the airborne measurements of the momentum flux of the longer waves with  $\lambda_x$  between 20 and 30 km reverse across the tropopause from negative values at lower to positive values at higher levels (Smith et al. 2008; Woods and Smith 2010). Another case of flux reversal across the tropopause was recently documented for coordinated research flights over Scandinavia (Gisinger et al. 2020, Fig. 10). Additionally, the airborne in situ measurements on board the German research aircraft High-Altitude Long-Range Research Aircraft (HALO) as well as in situ and remote sensing observations of the Doppler wind lidar (DWL) on board the DLR Falcon revealed the existence of a train of short gravity waves with  $\lambda_x \lesssim 10$  km extending  $\sim 300$  km downstream (Witschas et al. 2023).

 Denotes content that is immediately available upon publication as open access.

Corresponding author: Andreas Dörnbrack, andreas.doernbrack@dlr.de

DOI: 10.1175/JAS-D-24-0037.1

© 2024 American Meteorological Society. This published article is licensed under the terms of the default AMS reuse license. For information regarding reuse of this content and general copyright information, consult the AMS Copyright Policy ([www.ametsoc.org/PUBSReuseLicenses](http://www.ametsoc.org/PUBSReuseLicenses)).

TABLE 1. Times and locations of the two segments of the DLR Falcon research flights RF07 and RF08 as well as the four segments HL1–HL4 of the HALO research flight on 28 Jan 2016. Letters (a)–(f) refer to the profiles of the vertical displacements and vertical velocities along the respective flight legs as shown in Figs. 4 and A1. The simultaneous flight legs are in bold and correspond to the red lines in Figs. 4, 6, and A1.

	Flight leg	Time (UTC s)	Longitude (°E)	Latitude (°N)	Altitude (km)
(a)	RF07-FL2	52 390 ... 55 450	3.94 ... 17.07	61.18 ... 61.00	9.76 ... 9.81
(b)	<b>RF08-FL1</b>	<b>63 430 ... 67 540</b>	<b>16.48 ... 3.30</b>	<b>61.02 ... 61.18</b>	<b>9.77 ... 9.82</b>
(c)	<b>HL1</b>	<b>63 360 ... 67 479</b>	<b>17.41 ... 3.59</b>	<b>60.96 ... 61.03</b>	<b>7.76 ... 7.83</b>
(d)	HL2	67 934 ... 71 074	3.75 ... 16.41	61.05 ... 61.03	7.84 ... 7.79
(e)	HL3	72 089 ... 75 361	15.80 ... 3.59	59.43 ... 59.46	12.74 ... 12.72
(f)	HL4	76 294 ... 78 834	3.92 ... 16.73	61.05 ... 61.02	13.26 ... 13.30

Here, nonlinear numerical simulations are performed to determine whether a process similar to that proposed by Woods and Smith (2011), i.e., the secondary downward-propagating gravity waves generated by breaking mountain waves, can explain the occurrence of these short gravity waves. In doing so, the following research questions will be addressed and answered:

- 1) Does wave breaking occur over the Scandinavian mountains in numerical simulations applying a realistic high-resolution orography as lower boundary condition and ambient wind and stability conditions valid at the time of observation? Are downward-propagating secondary waves evident in the results of the numerical simulations?
- 2) Are downward-propagating gravity waves essential for the excitation and emergence of horizontally short modes in the TIL?
- 3) What are the characteristics of the simulated gravity waves near the tropopause?
- 4) What physical and numerical parameters determine the amplitude and wavelength of the short gravity waves in the TIL?

The paper is organized as follows. Section 2 presents briefly the research flights, the numerical model employed here to integrate the compressible equations for a deep atmosphere, and the global numerical weather prediction (NWP) model data. The NWP data are used in section 3 to explain the atmospheric flow and the conditions for mountain-wave propagation. Section 4 presents the vertical velocity spectra and the wave energy fluxes computed from the airborne measurements, and a brief interim summary and discussion is provided. The results of the numerical simulations including physical and numerical sensitivity studies are presented in section 5. Section 6 discusses the results and eventually draws conclusions.

## 2. Methodology

### a. Research flights

The research flights considered in this study were conducted over southern Scandinavia in the afternoon and evening of 28 January 2016. A detailed overview of the coordinated airborne observations by the DLR Falcon and the German research aircraft HALO is provided by Gisinger et al. (2020) in

their section 2.2.1. Here, Table 1 lists the times and coordinates of the six cross-mountain flight legs used in this study. The naming of the individual legs is the same as in Gisinger et al. (2020), who also provide a graphical overview of the flights in their Figs. 1 and 2.

Simultaneous observations on board the two aircraft were conducted on a flight path near 61°N from east to west where the DLR Falcon flew at 9.8-km altitude and HALO flew 2 km below from 1736 UTC until 1840 UTC: These are the research flight legs RF08-FL1 and HL1, respectively, highlighted in bold in Table 1. The RF07-FL2 research flight preceded these simultaneous flights, and HL2 followed them on the same route and flight levels assigned to each aircraft. The operation of the remote sensing instrument Gimballed Limb Observer for Radiance Imaging of the Atmosphere (GLORIA) required two high-level HALO legs at ~13-km altitude (HL3 and HL4) for probing the mountain waves over southern Scandinavia (Krisch et al. 2020).

### b. Numerical integrations

The nonlinear numerical simulations were conducted with the Eulerian/semi-Lagrangian (EULAG) fluid solver (Smolarkiewicz and Margolin 1997; Prusa et al. 2008). Here, the compressible Euler equations [Eqs. (1)–(4)] are integrated. The conservation laws for momentum, internal energy, and mass complemented by the ideal gas law are written in the symbolic coordinate-free form as presented by Smolarkiewicz et al. (2014):

$$\frac{d\mathbf{u}}{dt} = -c_p \theta \nabla \pi' - \mathbf{g} \frac{\theta'}{\theta_e} - \mathbf{f} \times \left( \mathbf{u} - \frac{\theta}{\theta_e} \mathbf{u}_e \right) - \alpha (\mathbf{u} - \mathbf{u}_e) + \mathbf{F}, \quad (1)$$

$$\frac{d\theta'}{dt} = -\mathbf{u} \cdot \nabla \theta_e - \beta \theta', \quad (2)$$

$$\frac{d\rho}{dt} = -\rho \nabla \cdot \mathbf{u}, \quad (3)$$

$$\pi = \left( \frac{R_d}{p_0} \rho \theta \right)^{R_d/c_v}. \quad (4)$$

Here, vector  $\mathbf{u}$  denotes the flow velocity,  $\theta$  is the potential temperature,  $\rho$  is the density, and  $\pi$  denotes the Exner function with the constant reference pressure  $p_0$ . The specific heat

at constant volume is related to the specific heat at constant pressure by  $c_v = c_p - R_d$ , where  $R_d$  is the gas constant for dry air. Absolute temperature is computed by  $T = \theta\pi$ , where the Exner pressure is defined as  $\pi \equiv (p/p_0)^\kappa$  and  $\kappa = R_d/c_p$ .

The magnitude of the gravitational acceleration is given by  $\mathbf{g} = (0, 0, -g)$ . The Coriolis parameter is given as  $\mathbf{f} \equiv 2\mathbf{\Omega}$ , where  $\mathbf{\Omega}$  denotes a constant angular velocity of the rotating reference frame. The differential operator of the material derivative in Eqs. (1)–(3) is defined as  $d/dt = \partial/\partial t + \mathbf{u} \cdot \nabla$ , where  $\nabla$  symbolizes the gradient operator. The operator  $\nabla \cdot$  in Eq. (3) refers to the divergence.

Equation (2) is written in perturbation form, i.e.,  $\theta' = \theta - \theta_e$  and  $\pi' = \pi - \pi_e$ ; see Smolarkiewicz et al. (2019). To facilitate the numerical solution, the auxiliary ambient states, sometimes called environmental states ( $\mathbf{u}_e, \theta_e$ ), are assumed to be known particular solutions of Eqs. (1) and (2). Generally, ambient states can be time dependent. In this paper, only  $z$ -dependent profiles ( $u_e, v_e, \theta_e, \rho_e$ ) are prescribed that automatically satisfy Eqs. (1) and (2). The ambient pressure  $p_e$  is computed from the ideal gas law equation [Eq. (4)] using an exponentially decreasing density  $\rho_e$  with a density scale height of 6500 m. For all numerical simulations, the initial conditions for the horizontal velocity components are identical to  $u_e$  and  $v_e$  and  $\theta'$  and  $w$  are set to zero.

The typical size of the computational domain in  $x, y$ , and  $z$  directions is 1008 km  $\times$  64 km  $\times$  70 km with spatial resolutions of 250 or 500 m. The lower boundary is free slip, and in the  $x$  direction, open boundaries with an additional Rayleigh damping of a width of 40 km on the inflow and outflow sides are used. In the  $y$  direction, cyclic boundaries are applied. Details for the individual numerical experiments can be found in Tables 3–6.

The terms in Eqs. (1) and (2) involving  $\alpha(\mathbf{x}, t)$  and  $\beta(\mathbf{x}, t)$  represent forcings to attenuate the solution to the prescribed environmental profiles  $\mathbf{u}_e$  and  $\theta_e$ . Here, the height-dependent amplitude damping of gravity waves is implemented as described in Prusa et al. (1996, section 3b). It emulates a diffusivity profile of the atmosphere whose attenuation rate increases exponentially with altitude throughout the computational domain, according to

$$\alpha = \beta = \tau^{-1} = \tau_{\text{MIN}}^{-1} \exp\left(\frac{z - z_{\text{top}}}{D_{\text{abs}}}\right), \quad (5)$$

where the quantity  $D_{\text{abs}}$  determines the vertical depth over which the diffusivity decreases to  $1/e$  from its full strength at the model top  $z_{\text{top}} = 80$  km. For the numerical simulations,  $D_{\text{abs}} \approx 10$  km is used, i.e., in the lowest 10–20 km of the computational domain, the exponential factor in Eq. (5) is nearly zero. This means that the amplitude of simulated vertically propagating mountain waves remains practically unaffected during the numerical integration in this area. For all simulations,  $\tau_{\text{MIN}} = 60$  s.

Equations (1)–(4) were implemented in the established geophysical flow solver EULAG (Prusa et al. 2008) as outlined by Smolarkiewicz et al. (2014). EULAG offers a variety of options to investigate the sensitivity of the solutions on numerical settings. Here, we differentiate between physical and numerical

sensitivity studies. The physical sensitivity is studied by varying the amplitude damping of the vertically propagating mountain waves to keep the numerical solution nearly linear (section 5a). In addition, the smoothness of the orography is varied and the strength of the TIL is enhanced in separated numerical integrations (sections 5b and 5c). In section 5d, the flow fields at  $t = 0$  are generated by a potential flow initialization and Eqs. (1)–(4) are integrated using the anelastic approximation; see Smolarkiewicz and Dörnbrack (2008), Smolarkiewicz et al. (2014) for details. Furthermore, we vary the stopping criteria of the elliptic solver (Smolarkiewicz et al. 1997), the distribution of processors used for the domain decomposition of the parallelized solver and test different options of the compiler (section 5d).

### c. Global NPW data

Operational analyses of the Integrated Forecasting System (IFS) of the ECMWF are used to provide meteorological data to characterize the atmospheric environment; these data will be denoted by HRES IFS. The model fields were taken from the suite of the IFS cycle 41r2 that became operational in March 2016. The IFS is discretized horizontally using a spherical harmonic expansion and a cubic-octahedral grid (Hólm et al. 2016). The TCo1279 resolution of the IFS cycle 41r2 uses 1279 total horizontal wavenumbers in the spherical harmonic expansion, resulting in an average 9-km horizontal resolution. In the vertical direction, 137 hybrid model levels cover the atmosphere from the surface up to the model top at 0.01 hPa. The IFS cycle 41r2 is the same as used for the most recent reanalysis data ERA5 (Hersbach et al. 2020). As ERA5, however, has a smaller resolution (TCo639), the operational analyses are used instead for the selected time period.

## 3. Atmospheric flow and conditions for the propagation of mountain waves

Figure 1 shows the height of the dynamical tropopause from the 1800 UTC HRES IFS analyses. Following the eastward passage of a narrow low pressure trough over southern Scandinavia between 1200 and 1800 UTC (still visible as nearly meridional band of low tropopause at the eastern edge of Fig. 1), an upper-level ridge formed, resulting in a fairly uniform tropopause between 8.5- and 9.5-km altitude. The upper-level flow was 25–30 m s<sup>-1</sup>, mainly from the west, and it can be considered as quasi steady during the research flights since there was no active weather system in the area.

Figure 2 supports the quasi steadiness of the upper-tropospheric and stratospheric flow by depicting hourly vertical profiles of various quantities taken at an upstream location in the interval from 1200 until 1800 UTC (different thin black lines) as well as their temporal mean (thick black line). The horizontal wind  $V_H$  increases from  $\sim 20$  m s<sup>-1</sup> near the ground to 60 m s<sup>-1</sup> at 30-km altitude; above this level,  $V_H$  is oscillating around a value of 60 m s<sup>-1</sup>, and in the upper stratosphere, the wind is decreasing slightly to values of  $\sim 40$  m s<sup>-1</sup> (Fig. 2a). The wind direction turns from west-southwesterlies to westerlies in the troposphere, turns back to west-southwesterlies again in the

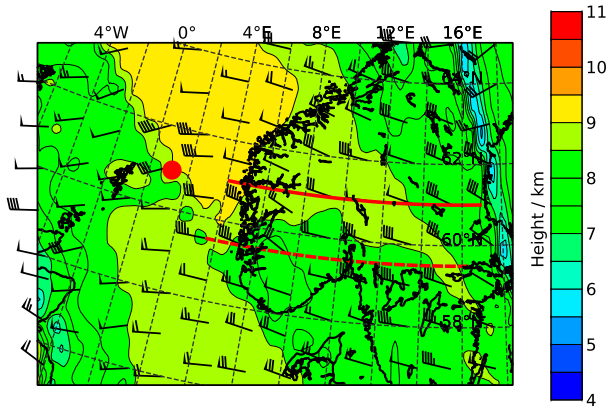


FIG. 1. Height of the dynamical tropopause (km; color shaded) and horizontal wind vectors ( $\text{m s}^{-1}$ ; barbs) at the 2 PVU ( $1 \text{ PVU} = 10^{-6} \text{ K kg}^{-1} \text{ m}^2 \text{ s}^{-1}$ ) surface for 1800 UTC 28 Jan 2016. Data: IFS HRES operational analysis. The solid red lines mark the flight track of the DLR Falcon and the HALO legs HL1, HL2, and HL4; the dashed red line marks that of HL3. The red dot denotes the location where the upstream profiles shown in Fig. 2 are taken.

stratosphere up to  $\sim 30$  km, and, finally, becomes nearly westerly above (solid line in Fig. 2b).

Overall, the vertical profile of the buoyancy frequency  $N(z) = g\partial \ln\theta/\partial z$  can be approximated by two characteristic values distinguishing the troposphere  $N = N_T = 0.01 \text{ s}^{-1}$  and the stratosphere  $N = 0.018 \text{ s}^{-1} \approx N_S = 0.02 \text{ s}^{-1}$  (solid lines in Fig. 2c). However, there are two important deviations from a textbook two-layer  $N(z)$ -profile marked by enhanced static stabilities. First, the narrow, approximately 2-km deep TIL at an altitude of around 10 km shows maximum  $N$  values of  $0.025 \text{ s}^{-1}$ . The formation of the TIL is associated with the high-pressure tropospheric ridge mentioned above and is commonly

found under these anticyclonic atmospheric conditions (Wirth 2001). Second, and due to the temperature increase with altitude, the layer below the stratopause reaches maximum  $N$  values of  $0.026 \text{ s}^{-1}$  over approximately 15-km depth.

Of particular importance is the profile of the approximated Scorer parameter  $\ell = \sqrt{N^2/U^2}$  corresponding to a cutoff wavenumber  $\ell = k_c = 2\pi/\lambda_c$  that separates propagating from evanescent linear wave modes (Fig. 2d). Both in the troposphere and in the lower stratosphere,  $\ell$  decreases with altitude providing suitable conditions for tropospheric as well as stratospheric wave ducting and trapping (Danielsen and Bleck 1970).

The smallest cutoff wavelengths  $\lambda_c \approx 6\text{--}8$  km appear directly at the TIL (unsurprisingly, as  $N$  maximizes). In other words, as soon as mountain waves are excited, only upgoing waves with  $\lambda_x > \lambda_c$  can propagate vertically, and all shorter modes become evanescent and do not penetrate the thick layer of enhanced  $\lambda_c$  underneath the TIL. Higher up,  $\lambda_c$  increases with altitude up to  $\sim 20$  km, i.e., gradually longer waves reach their turning levels and are reflected downward, which is consistent with previous linear studies of deep propagating mountain waves (Schoeberl 1985).

The large-scale atmospheric response to the strong flow from the west-southwest over the Scandinavian mountains is illustrated by the simulated wave-induced temperature perturbations  $T'$  derived from the HRES IFS. Here, advantage is taken of the spectral IFS, and the absolute temperature  $T$  is obtained with two spectral truncations, TCo1279 and TCo106, interpolated to the same latitude/longitude grid. The difference between the two  $T$  fields represents the temperature perturbations  $T'$  as shown in Fig. 3.

Near the tropopause at 250 hPa and in the lower stratosphere at 150 hPa (Figs. 3a,b), gravity waves with  $T'$  amplitudes larger than 2 K are only present over Scandinavia. The amplitude enhancement over the mountains and their

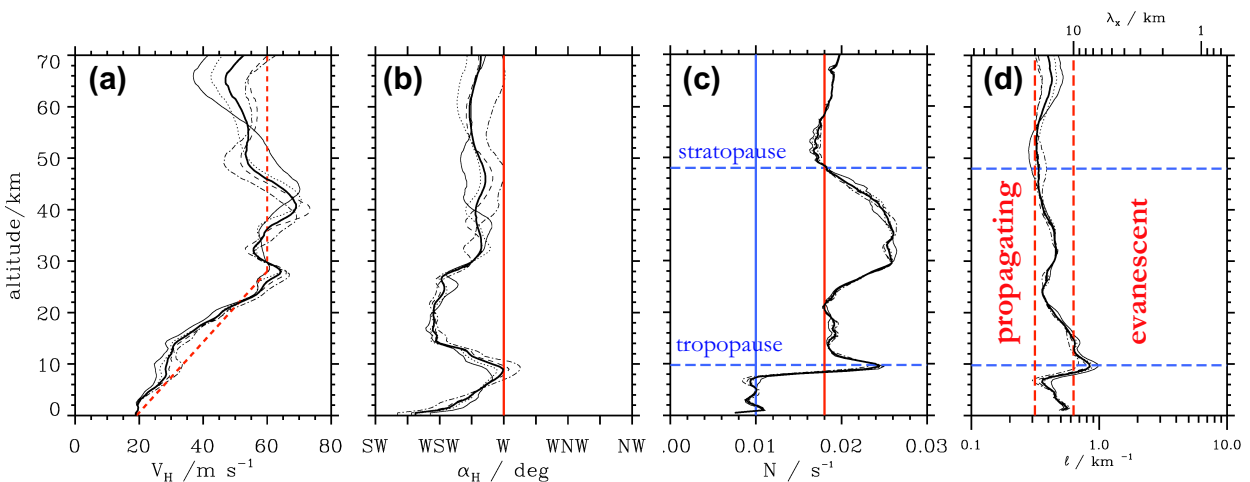


FIG. 2. Upstream profiles taken at  $61^\circ\text{N}$  and  $1^\circ\text{E}$  (red dot in Figs. 1 and 3) of (a) horizontal wind  $V_H$ , (b) wind direction  $\alpha_H$ , (c) buoyancy frequency  $N$ , and (d) scorer parameter  $\ell$  for 1200, 1400, 1600, and 1800 UTC (thin black lines: solid, dotted, dashed, and dash-dotted, respectively) and as temporal mean (thick solid lines) for 28 Jan 2016. Data: Spectrally truncated T21 IFS HRES operational analyses and short-term forecasts initialized at 1200 UTC. The red and blue lines mark features mentioned in the text.

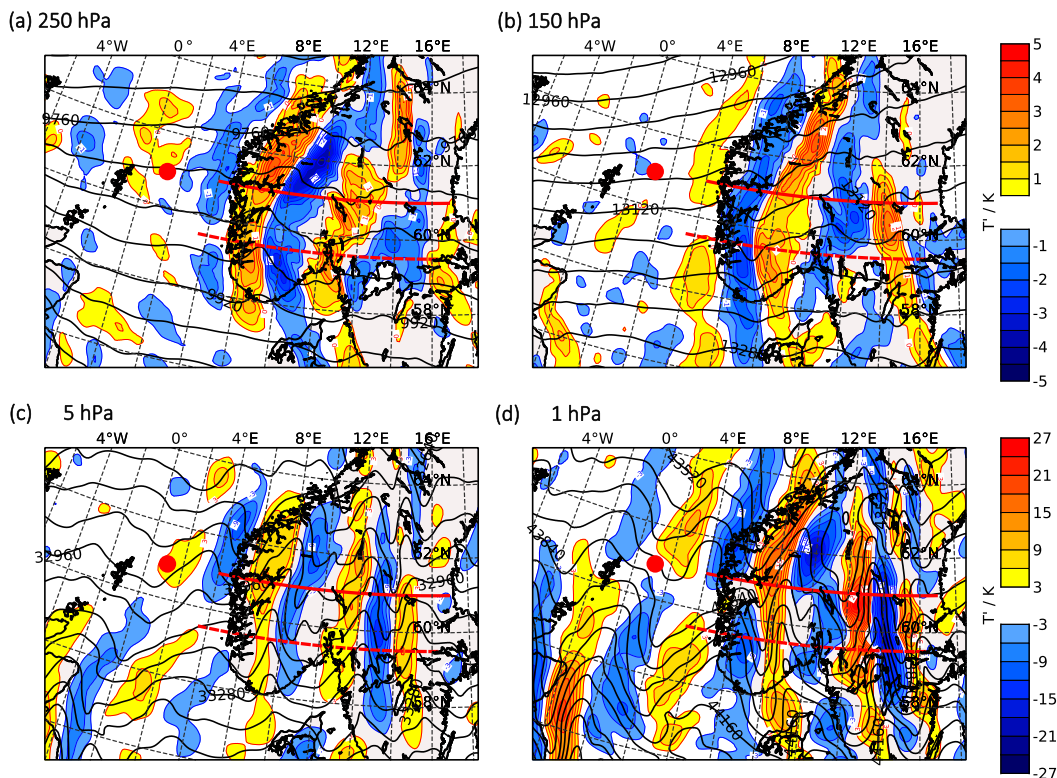


FIG. 3. Temperature perturbations  $T' = T_{T1279} - T_{T106}$  on the 250-, 150-, 5-, and 1-hPa pressure surfaces at 1800 UTC 28 Jan 2016. Black contour lines: geopotential height in meters. Data: IFS HRES operational analysis. The solid red lines mark the flight track of the DLR Falcon and the HALO legs HL1, HL2, and HL4; the dashed red line marks that of HL3. The red dot denotes the location where the upstream profiles shown in Fig. 2 are taken.

phase alignment with the orographic barrier point to their orographic origin. Their horizontal wavelengths are  $300 \pm 30$  km at  $60^\circ\text{N}$ . Between the two pressure levels, the phase of  $T'$  is shifted by  $\sim 180^\circ$  indicating the upstream tilt of the simulated mountain waves into the ambient wind. From the height of the pressure surfaces (black contour lines in Fig. 3), a vertical wavelength  $\lambda_z \approx 6$  km can be estimated. Assuming a horizontal wind of  $30 \text{ m s}^{-1}$  (see Fig. 2a), an intrinsic frequency  $\omega \approx 6.28 \times 10^{-4} \text{ s}^{-1}$  is estimated. It is orders of magnitude smaller than  $N$  (see Fig. 2c) and by a factor  $\sim 5$  greater than the Coriolis parameter  $f$  at this latitude. Thus, these internal gravity waves are essentially inertia gravity waves excited by the flow across the Scandinavian mountains. Their spatial structure resembles those analyzed by Dörnbrack et al. (2002).

These hydrostatic mountain waves are well resolved by the IFS and confirm the predictions of favorable propagation conditions based on the Scorer parameter; see Fig. 2d. The upper stratospheric levels in Figs. 3c and 3d reveal that these mountain waves propagate into the middle atmosphere where the  $T'$  amplitude increases to values larger than 15 K due to the decreasing density. The contour lines of the geopotential height show large meridional deflections, which point to a significant mountain-wave-induced disturbance of the zonal flow.

#### 4. Airborne observations of vertical velocity, spectra, and energy wave fluxes

##### a. Airborne observations

Figure 4 shows the vertical displacements  $\eta = \int_W^x w'(x)/U(x)dx$ , where the perturbations of the vertical wind  $w'$  are determined from the in situ measurements as suggested by Smith et al. (2016) and  $W$  denotes the westernmost waypoints of the six cross-mountain legs. The  $w$  profiles as observed by the DLR Falcon and HALO are added as Fig. A1 in the appendix, where the individual measurement systems are also referenced. As all flights legs were nearly parallel to the zonal wind  $U$  (see Fig. 2b), the different  $\eta$  profiles in Fig. 4 reveal the observed large-scale and small-scale flow response in the upper troposphere, near the tropopause, and in the lowermost stratosphere. Based on the visual impression of these measurements and as a practical convention, the cross-mountain legs are divided into three segments: (i) an upstream segment from the westernmost waypoints to  $7.5^\circ\text{E}$ , (ii) a ridge segment from  $7.5^\circ$  to  $11.5^\circ\text{E}$ , and (iii) a downstream segment east of  $11.5^\circ\text{E}$ ; see the vertical dashed lines in the upper panel of Fig. 4.

In addition to the ubiquitous presence of gravity waves with  $\lambda_x \lesssim 10 \text{ km}$ , the lower  $\eta$  profiles show a mountain wave, in particular in the HALO leg HL1 [profile (c) in Fig. 4],

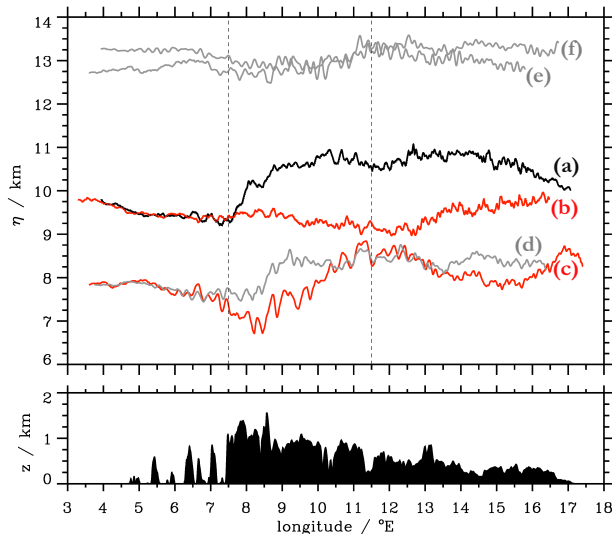


FIG. 4. (top) Vertical displacements  $\eta$  for the six cross-mountain legs of the research flights of DLR Falcon and HALO as listed in Table 1. The line colors correspond to the ones used in Fig. A1. The vertical dashed lines mark the boundaries between the upstream, ridge, and downstream segments. (bottom) ASTER orography at around 61°N underneath FL2 of RF07.

whose horizontal wavelength can be estimated to be  $\sim 6^\circ$ . This corresponds to  $\lambda_x \approx 330$  km and is in very good quantitative agreement with the wavelength of the mountain wave as estimated from the simulated  $T'$  values of the IFS, as shown in section 3. The horizontally longwave is also discernible in both stratospheric legs flown by HALO along about 60°N [profile (e) in Fig. 4] and along  $\sim 61^\circ$ N [profile (f) in Fig. 4]. However, their amplitude is smaller at the higher flight levels. Since both legs are displaced in the north–south direction, the apparent coherence of the  $\eta$  profiles supports the quasi two dimensionality of the large-scale wave response in agreement with the previous findings from the IFS (cf. Fig. 3).

The  $\eta$  profiles in the upstream segments of the DLR Falcon [profiles (a) and (b) in Fig. 4] as well as of the HALO legs [profiles (c) and (d) in Fig. 4] are very similar. Here, it should be noted that the time difference of the observations was  $\sim 4$  h in the case of the DLR Falcon but only a few minutes by the HALO research flights. This pronounced agreement of the  $\eta$  profiles suggests a high degree of steadiness in the upstream flow. Over the mountains, however, the  $\eta$  profiles deviate due to mountain waves that alter both the horizontal and vertical wind fields with time. The vertical displacements calculated for two DLR Falcon legs differ markedly in the ridge and downstream segments, indicating a transient airflow induced by the mountain waves.

The only simultaneous observations were performed by DLR Falcon [RF08-FL1 at 9.8-km altitude, profile (b)] and by HALO [HL1 at 7.9-km altitude, profile (c)] and are marked in red in Figs. 4 and A1. Visual impression suggests irregular, low-amplitude oscillations west of 6.5°E, which become more distinct wave signals over the fjords at  $\sim 7.5^\circ$ E in the upstream

segment. Over the mountains, horizontally longer waves with larger  $w$  amplitudes up to  $\sim 2$  m s $^{-1}$  dominate up to 12°E (Fig. A1). Here, the signatures of these longer waves are clearly visible in the lower leg HL1. Finally, further east, horizontally shorter waves with considerable amplitudes  $> 3$  m s $^{-1}$  predominate.

Overall, it is difficult to relate individual short-wave patterns in the two simultaneous legs, suggesting a pronounced vertical change in their wave characteristics over the  $\sim 2$  km between the two flight levels. In addition, the short-wave response is very transient when comparing the DLR Falcon legs at different times [profiles (a) and (b) in Figs. 4 and A1]. It is hardly possible to identify a wave pattern with the same phase at a specific location. This means that transient gravity waves probably existed during the 3–4 h between measurements. An analogous conclusion can be drawn by comparing the two HALO legs HL1 and HL2, which are separated by a maximum of 1 h at the eastern waypoints. Here, some similarities in the wave phases between 6.5° and 8.5°E and around 11°E can be observed. Nevertheless, both profiles (c) and (d) in Figs. 4 and A1 demonstrate a pronounced unsteadiness in the short-wave response. Profiles (e) and (f) in Figs. 4 and A1 show the uppermost HALO observations along legs HL2 and HL3: the larger amplitudes and longer horizontal wavelengths of the short gravity waves are the most obvious features of these measurements, which cover almost all segments. Again, as with the lower legs, there are no concurrent phase matches of these short gravity waves in the measurements along these legs.

On the DLR Falcon, a scanning DWL also measured the wind below the aircraft (Witschas et al. 2017). The observations of the vertical wind for the flight legs RF07-FL2 and RF08-FL1 are depicted in Fig. 5 and those of the horizontal wind along the RF08-FL1 leg in Fig. A2 of the appendix. A common feature of both DLR Falcon flight legs is a band of nearly continuous observations from 9.5 km down to  $\sim 8$ -km altitude (Figs. 5a,b), below which dense clouds prevented further lidar measurements. In regions of lower cloud cover, as occurred upstream of the main ridge, the laser beam was able to penetrate to lower altitudes.

The DWL data are the same as those used for Figs. 8 and 9b of Gisinger et al. (2020) and for the momentum flux analysis of Witschas et al. (2023). Moreover, lines of constant potential temperature calculated from the IFS-HRES data and spatiotemporally interpolated to the flight paths are superimposed here. First, these plots show that the DLR Falcon in situ flight observations [Figs. 4 and A1, profiles (a) and (b)] were made directly in the TIL and the lowermost stratosphere, where the static stability (densely packed isentropes in Fig. 5) is very high. Second, the DWL vertical winds show nearly vertical phase lines, indicating evanescent modes trapped in the TIL and upper troposphere.

Figure 5a shows narrow wave trains just beneath the flight level with small amplitudes in the upstream segment during RF07-FL2. Their depth is limited to  $\sim 1$  km, and there is no obvious connection to lower levels. During RF08-FL1 and about 4 h later, the DWL reveals gravity waves extending to lower altitudes; see Fig. 5b. The individual up- and downdrafts of the

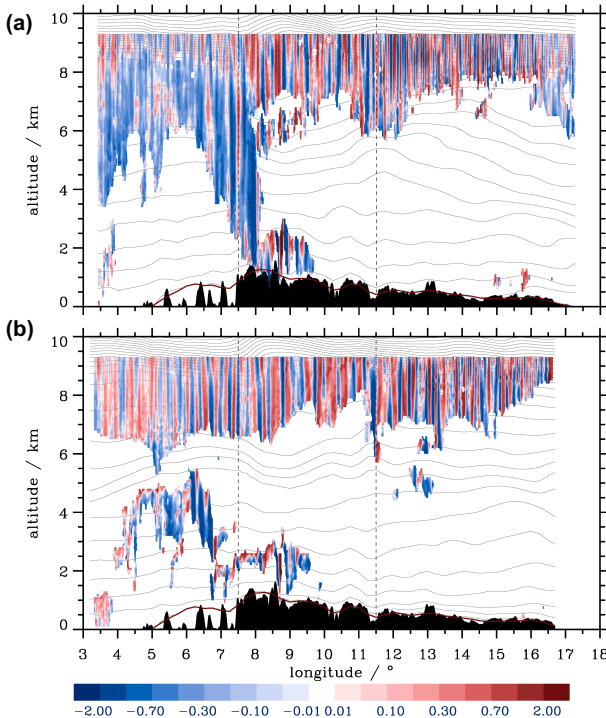


FIG. 5. (a) Observed vertical velocity ( $\text{m s}^{-1}$ ; color shaded, nadir-pointing DWL, 1-s resolution data smoothed with a 10-s filter) and IFS potential temperature (K; contour lines; 2-K intervals) interpolated along the flight track RF07-FL2. (b) Observed vertical velocity ( $\text{m s}^{-1}$ ; color shaded; forward-backward scanning DWL; 5-s resolution data smoothed with a 10-s filter) and IFS potential temperature (K; contour lines; 2-K intervals) interpolated along the flight track RF08-FL1. ASTER orography underneath the flight path in black. The reddish-brown line marks the IFS orography.

gravity waves are now broader, and the few measurements in the lower troposphere indicate that they are not directly connected to the orographic sources in the fjord region of the upstream segment; see the updrafts at around  $6^{\circ}$ – $7^{\circ}$ E. In the ridge segment, the waves extend lower into the troposphere, and especially over the highest mountains, the waves appear to be related to the forcing from the flow over the individual peaks; see the region around  $8.5^{\circ}$ E in Figs. 5a and 5b. Their amplitudes are larger, and the horizontal wavelength is longer than that of the upstream waves. Further downstream, the individual up- and downdrafts in the TIL and upper troposphere become thinner, i.e., their horizontal wavelength shrinks and the vertical extent of these apparently horizontally compressed wave trains is difficult to estimate. However, the downward decreasing amplitude of the observations in the downstream segment near the easternmost waypoint of RF07-FL2 indicates that they probably do not extend to lower levels. Indeed, the thermal stratification as shown by the IFS isentropes suggests that their vertical extent is related to the existence of stably stratified layers (cf. also patterns in the upstream segment of RF07-FL2). The horizontal wind observations by the DWL along RF08-FL1 reveal a long mountain wave (Fig. A2) corresponding to a potential temperature

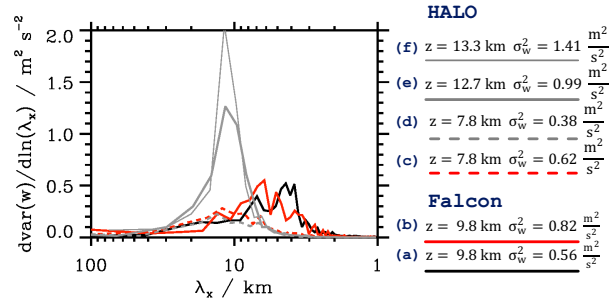


FIG. 6. Binned energy spectra of the vertical velocity from research flights of DLR Falcon and HALO. (a) RF07-FL2, (b) RF08-FL1, (c) HL1, (d) HL2, (e) HL3, and (f) HL4. The red legs mark simultaneous measurements, the legs marked with dashed lines are taken at the same flight leg and altitude, and the solid gray lines mark the upper-level legs of HALO.

minimum directly over the ridge section. The position and the amplitude are reasonably well reproduced by the HRES IFS. Its phase and wavelength also correspond nicely to the coarse-grain GLORIA measurements as analyzed by Kriscit et al. (2020).

b. Energy spectra

The spectral power of the vertical wind as measured by both aircraft is shown in Figs. 6 and 7. The binned energy spectra of the two DLR Falcon legs show maxima between  $\lambda_x \approx 4$  and 7 km (red and black solid lines in Fig. 6). The lower HALO legs HL1 and HL2 (dashed lines in Fig. 6) exhibit a broader distribution with smaller maximum amplitudes between  $\lambda_x \approx 10$  and 20 km. The upper HALO legs HL3 and HL4 also peak in this wavelength range but reach spectral amplitudes 5–8 times higher than the maxima at 7.8-km altitude. This altitude dependence is also reflected in the variances  $\sigma_w$  averaged over the legs, which increase from the upper troposphere (HL1 and HL2) and TIL region (RF07-FL2 and RF08-FL1) toward the uppermost HALO levels of legs HL3 and HL4 in the lower stratosphere. In addition to the 1-Hz data as used for the legs shown in Fig. 6, the spectra computed with the 10-Hz data for RF07-FL2 and RF08-FL1 show a similar shape (dotted curves), confirming the previous analysis.

Below the DLR Falcon flight level, the vertical dependency of the spectral energy content between 7.9- and 9.1-km altitude was analyzed using the DWL observations of  $w$  at selected levels; see Fig. 7. The spectral distribution of the earlier flight RF07-FL2 is characterized by enhanced amplitudes in the range from  $\lambda_x \approx 4$  to 30 km (Fig. 7a). Individual spectral peaks are located at  $\lambda_x \approx 5$  and 10 km. The maximum values of the DWL observations are up to a factor 4 smaller than the values calculated from the in situ measurements at flight level (black line in Fig. 7a). This drop in amplitude and in  $\sigma_w$  from the DLR Falcon flight level down to an altitude of 8–9 km could indicate evanescent gravity waves trapped in the TIL.

The spectral distribution for the second flight RF08-FL1 is slightly different: the amplitude has increased and the energy is shifted to longer  $\lambda_x$  in accordance with the visual impression

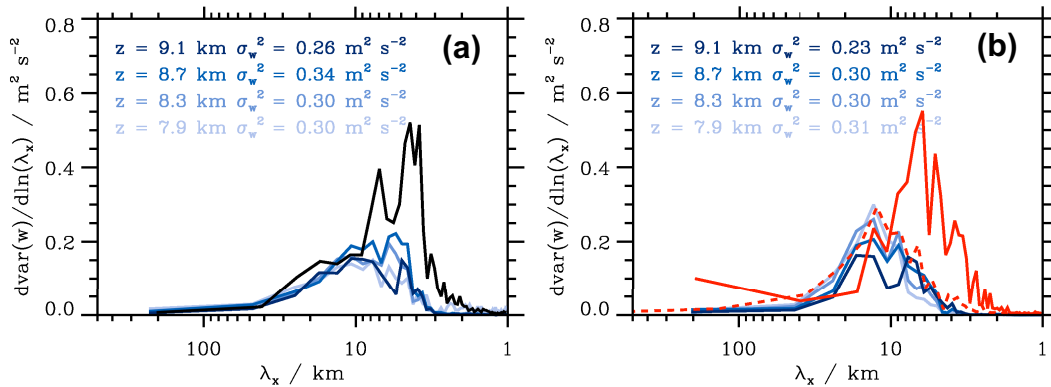


FIG. 7. Binned energy spectra of the vertical velocity measured by the DWL from DLR Falcon research flights (a) RF07-FL2 and (b) RF08-FL1 at selected vertical levels beneath the flight path. Their gray shading becomes darker with increasing altitude. The solid black lines in (a) and solid red lines in (b) are the  $w$  spectra from the DLR Falcon in situ measurements at 9.8-km altitude. The dashed red line in (b) is from the simultaneous HALO in situ flight at 7.8-km altitude along HL1.

of Fig. 5. At 9.1-km altitude, short modes with  $\lambda_x \approx 8$  km are clearly separated from somewhat longer modes at  $\lambda_x \approx 12$  km. At the lower vertical levels, only these longer gravity waves dominate and the distribution is unimodal, a finding that is confirmed by the nearly simultaneous in situ observations from HALO at 7.8-km altitude along HL1 (red dashed line in Fig. 7b). As in the previous DLR Falcon flight leg RF07-FL2, the spectral distribution in the TIL is dominated by gravity waves between  $\lambda_x \approx 3$  and 8 km.

Together with the visual impression of Fig. 5, the results presented in Figs. 6 and 7 provide a consistent picture: horizontally short modes with  $\lambda_x < 10$  km are mainly present in a layer from  $\sim 8$ - to 10-km altitude. Their  $\lambda_x$  decrease and their amplitudes increase upward. Very short modes with  $\lambda_x < 5$  km occur mainly in the ridge and downstream segments. Above the TIL, the two HALO observations indicate the existence of horizontally longer modes with  $\lambda_x > 10$  km. Below the TIL, it is difficult to obtain a coherent picture from the DWL plots alone. However, the few instances where the DWL could observe almost the entire troposphere suggest that the gravity waves have horizontal wavelengths  $\lambda_x \gtrsim 20$  km associated with the flow across individual mountain peaks.

### c. Wave energy fluxes

From the flight level in situ observations, local perturbations  $\varphi'$  ( $\varphi = u, v, w, p$ ) are calculated by subtracting mean values  $\langle \varphi \rangle$  as a moving average:

$$\langle \varphi \rangle = \frac{1}{L} \int_{-L/2}^{L/2} \varphi dx \quad \text{with } \varphi = u, v, w, p, \quad (6)$$

over a specified length  $L$ . Two scales ( $L = 20$  and 300 km) are chosen to focus on flux contributions from horizontally shorter and longer waves. In the following, we present the three components of the wave energy flux vector  $\text{EF}_x = \langle u'p'_c \rangle$ ,  $\text{EF}_y = \langle v'p'_c \rangle$ , and  $\text{EF}_z = \langle w'p'_c \rangle$ , where  $p_c$  is the observed static pressure  $p$  corrected to a constant reference altitude  $z_{\text{ref}}$  assuming

hydrostatic balance  $p_c(x) = p(x) + \bar{\rho}g(z - z_{\text{ref}})$ . Here,  $z$  is the aircraft geometric altitude determined from the global positioning system (GPS) and  $\bar{\rho}$  is the leg-averaged density (Smith et al. 2008, 2016).

In general, the wave energy flux vector determines in which direction and at which rate energy is being transported by the wave motion (Dutton 1976, section 12.4.3). Furthermore, the Eliassen–Palm relation provides a functional relation between the vertical flux of wave energy  $\text{EF}_z$  and the negative scalar product of the vectors of the horizontal wind  $\mathbf{U}$  and the momentum flux  $\mathbf{MF} = (\text{MF}_x, \text{MF}_y) = (\bar{\rho}\langle u'w' \rangle, \bar{\rho}\langle v'w' \rangle)$  as

$$\text{EF}_z = -\mathbf{MF} \cdot \mathbf{U}. \quad (7)$$

According to Eliassen and Palm (1961),  $\text{EF}_z$  and  $-\mathbf{MF} \cdot \mathbf{U}$  should be directly proportional for linearly propagating, stationary, nondissipative mountain waves. Figure 8 shows the wave energy fluxes from both DLR Falcon legs for  $L = 20$  km. The  $\text{EF}_z$  and  $-\mathbf{MF} \cdot \mathbf{U}$  oscillate around zero and achieve local maxima and minima of over  $5 \text{ W m}^{-2}$  for distances  $x > 250$  km, i.e., over the mountains and downstream. For both legs, these independently determined fluxes are largely in phase and correlation coefficients of 0.745 and 0.875 were computed, respectively. However, while the Eliassen–Palm relation holds in the first 250 km, the amplitude and phase difference between  $\text{EF}_z$  and  $-\mathbf{MF} \cdot \mathbf{U}$  increase over the mountains and downstream. This deviation indicates transient and nonlinear processes that violate the assumptions for which Eq. (7) was derived, which is consistent with the 3D results of Woods and Smith (2011). The alternating sequence of positive and negative vertical energy fluxes indicates that upward- and downward-propagating short waves occur at the same time. Averaged over the entire cross-mountain leg, the vertical energy fluxes for  $L = 20$  km for both DLR Falcon legs are negative and amount to  $-1.15$  and  $-1.53 \text{ W m}^{-2}$ , respectively, which is another indication that downward-propagating short gravity waves can be detected; see Table 2.



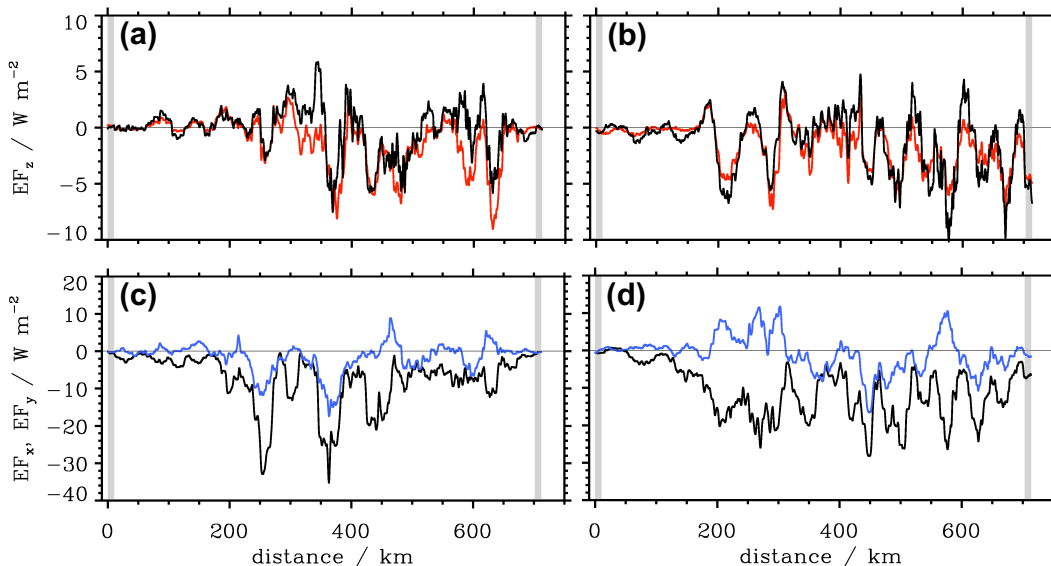


FIG. 8. (a),(b) Vertical energy fluxes  $EF_z$  as well as  $-\mathbf{MF} \cdot \mathbf{U}$  [red and black lines in (a) and (b)] and (c),(d) horizontal energy fluxes  $EF_x$  and  $EF_y$  [black and blue curves in (c) and (d)] along DLR Falcon research flights (left) RF07-FL2 and (right) RF08-FL1 calculated from the flight level in situ data using moving averages of  $L = 20$  km.

The zonal energy flux  $EF_x$  is always negative indicating that the detected waves are propagating against the mean westerly flow at this altitude (cf. Fig. 3b). The meridional component  $EF_y$  is smaller and fluctuates around zero. In the nearly zonal flow, one would expect that a positive  $EF_z$  correlates with negative  $EF_x$  for stationary, upward-propagating mountain waves. This clear correspondence valid for linearly upward-propagating waves cannot be observed for short gravity waves as detected along the both DLR Falcon flight legs as shown in Fig. 8.

Analysis of the horizontally longer waves with filter length  $L = 300$  km gives a small positive vertical energy flux  $EF_z$  of  $0.28 \text{ W m}^{-2}$  for the first DLR Falcon leg, a likewise small but negative value of  $-0.14 \text{ W m}^{-2}$  for the second DLR Falcon leg; see Table 2. Here, the zonal wave energy fluxes  $EF_x$  are clearly negative, and their absolute values are larger than their short-wave counterparts. As before, the meridional flux values  $EF_y$  are smaller and the sign change between the two legs of the DLR Falcon might be related to the gradually

turning wind at this level; see Fig. 2b. These results indicate that the longer mountain waves propagated upward, but that this wave propagation gradually weakened or ceased until the combined DLR Falcon and HALO flights.

The simultaneous HALO flight HL1 also revealed negative energy fluxes  $EF_z$  for both filter lengths; see Table 2. This quantitative evaluation of vertical energy fluxes suggests that upward- and downward-propagating waves coexist near the tropopause and also in the upper troposphere where HALO flew. Concordantly, both HALO legs HL3 and HL4 in the lower stratosphere yield downward-propagating short waves with  $EF_z \leq -1 \text{ W m}^{-2}$ . Surprisingly, the contribution of longer waves does not deliver a systematic picture of predominantly upward-propagating mountain waves, again suggesting temporal variability in the airborne observations; see Table 2. Altogether, it must be noted that the  $EF_z$  is small compared to strong mountain-wave events as found over New Zealand’s Southern Alps (Smith et al. 2016) or over the Southern Andes (Dörnbrack et al. 2022b).

TABLE 2. Averaged energy fluxes for the two legs of the DLR Falcon research flights RF07 and RF08 as well as the four legs HL1–HL4 of the HALO research flight on 28 Jan 2016. Letters (a)–(f) refer to the lines in Table 1 as well as to profiles in Figs. 4 and A1. The simultaneous flight legs are in bold. The two comma-separated numbers refer to average lengths of  $L = 20$  and  $300$  km, respectively.

	Flight leg	$EF_z \text{ (W m}^{-2}\text{)}$	$-\mathbf{U} \cdot \mathbf{MF} \text{ (W m}^{-2}\text{)}$	$EF_x \text{ (W m}^{-2}\text{)}$	$EF_y \text{ (W m}^{-2}\text{)}$
(a)	RF07-FL2	-1.15, 0.28	-0.18, 1.75	-7.61, -111.75	-1.61, 22.70
(b)	<b>RF08-FL1</b>	<b>-1.53, -0.14</b>	<b>-1.28, 0.20</b>	<b>-11.10, -90.30</b>	<b>-0.68, -14.26</b>
(c)	<b>HL1</b>	<b>-0.38, -0.24</b>	<b>-0.12, 0.67</b>	<b>-2.17, -22.10</b>	<b>-0.55, -2.16</b>
(d)	HL2	-0.23, 0.66	-0.11, 0.66	-1.94, -32.34	-0.19, -1.70
(e)	HL3	-1.00, -0.11	0.49, 1.07	-3.51, -32.04	-2.15, -8.02
(f)	HL4	-1.19, 0.81	0.31, 1.12	-6.82, -38.41	-0.49, 3.22

#### d. Interim summary and discussion

Combining the airborne observations with the IFS analysis presented in the previous sections reveals that horizontally longer mountain waves propagate predominantly upward. Their energy and momentum fluxes are small. However, the most striking feature of the airborne observations is the occurrence of internal gravity waves shorter than 10 km near the tropopause. Not exclusively, but the shortest modes can be found clustered in the lee of the Scandinavian mountains. These short modes are absent both further down in the upper troposphere and further up in the lower stratosphere.

It could not be proved incontrovertibly that these waves are stationary mountain waves. Instead, the analysis to this point, especially, the observed phase differences of  $\eta$  and  $w$  along RF07-FL2 and RF08-FL1, suggests that these short waves are transient and unsteady. It should be noted that the same diagnostic tools were earlier applied to determine upward-propagating mountain waves uniquely, e.g., [Smith et al. \(2008, 2016\)](#), [Bramberger et al. \(2017\)](#), [Dörnbrack et al. \(2022b\)](#). The above interim conclusions are supported by the earlier studies of [Gisinger et al. \(2020\)](#), [Krisch et al. \(2020\)](#). There, the low values of the observed momentum fluxes are interpreted as a sign for evanescent and trapped waves in agreement with the findings regarding the energy fluxes of this study. However, the question where these short waves come from and how they were excited has not been answered yet. An attempt to answer this question will be made in the next sections.

Based on linear wave theory, however, can we understand these results? Atmospheric airflow over complex terrain excites a broad spectrum of mountain waves ([Smith and Kruse 2017](#)). First, we assume that the short waves in the TIL result directly from the airflow across the rugged Scandinavian terrain (see the profile of the orography in the lower panel of [Fig. A1](#)). For sake of simplicity, let us consider a single harmonic mode with horizontal wavenumber  $k = 2\pi/\lambda_x$ , where  $\lambda_x$  is either 5 or 7 km corresponding to the short waves found in the DLR Falcon measurements. To allow for vertically propagating modes, a uniform flow of  $u_0 = 20 \text{ m s}^{-1}$  would require buoyancy frequencies  $N$  larger than 0.025 or 0.018  $\text{s}^{-1}$  for these 5- or 7-km waves ([Durrán 1990](#), Eq. 4.23). If one increases  $u_0$  by 10  $\text{m s}^{-1}$ , the limiting buoyancy frequencies would also increase to 0.038 or 0.027  $\text{s}^{-1}$ , respectively. These values are much larger in comparison with the  $N$  values of  $\sim 0.01 \text{ s}^{-1}$  characteristic for the upstream conditions on this day and as shown in [Fig. 2c](#). Therefore, it is highly unlikely that these short waves will propagate through the troposphere to the TIL, provided that wind and thermal stratifications are uniform.

But there are the evanescent modes. Let us again assume uniform zonal velocities  $u_0$  of 20 or 30  $\text{m s}^{-1}$  and a constant tropospheric  $N = 0.01 \text{ s}^{-1}$ . Then, evanescent modes of horizontal wavenumber  $k$  exist if  $u_0 k > N$  and the corresponding wave amplitude decays proportional to an attenuation factor  $e^{-\mu z}$  with the vertical decay rate  $\mu = \sqrt{k^2 - N^2/u_0^2}$  ([Durrán 1990](#), Eq. 4.23). In the lower troposphere, the airflow shall excite evanescent modes at wavenumbers  $k_1 = 2\pi/5 \text{ km}$  and

$k_2 = 2\pi/7 \text{ km}$ . How much does the amplitude attenuate over a vertical distance of 10 km to the TIL? The amplitude of the 5-km wave has attenuated to less than 0.001% of its original value; for the longer wave, it is 0.06% for  $u_0 = 20 \text{ m s}^{-1}$  and 0.02% for  $u_0 = 30 \text{ m s}^{-1}$ . This result suggests that short evanescent waves are unlikely to affect TIL significantly under the above assumptions.

However, the decrease of the Scorer parameter  $\ell$  as shown in [Fig. 2d](#) reflects the strong tropospheric shear during the time of the observations. As discussed by [Schoeberl \(1985\)](#), stationary mountain waves reach their turning level when the intrinsic frequency  $\omega = -u_0 k$  equals the buoyancy frequency  $N$ , or in other words when their vertical wavelength (wavenumber) increases (decreases) (e.g., [Fritts and Alexander 2003](#), section 3.2.2). There, only waves with  $\lambda_x > \lambda_c$  may propagate freely further upward; all other shorter waves are being reflected and are trapped or ducted and might create a resonant leewave train. The short, high-frequency gravity waves have intrinsic frequencies near  $N$ . In contradiction to the case with constant wind, the wave amplitude only decays gradually in the duct resulting in large vertical velocities. As a further result, these waves have little or no associated vertical flux of horizontal momentum ([Fritts and Alexander 2003](#); [Smith and Kruse 2017](#)).

Wurtele's one-layer Couette-flow model for constant stability and constant shear ([Queney et al. 1960](#), p. 64) can be easily applied to estimate the free propagating modes and the number of discrete resonant modes. The dashed line in [Fig. 2a](#) indicates a mean shear of  $40 \text{ m s}^{-1} (30 \text{ km})^{-1} = 10 \text{ m s}^{-1} (7.5 \text{ km})^{-1}$ . The tabulated numerical solutions of Wurtele's linear wave equation for depths of 6, 8, 10, and 12 km over which the wind increases to  $10 \text{ m s}^{-1}$  provide the minimum wavelengths of the free waves. For a shear of  $10 \text{ m s}^{-1} (8 \text{ km})^{-1}$ , the shortest wavelength is 10 km and the number of resonant modes is 6. The numerical solutions also reveal that increasing shear makes  $\lambda_x$  larger and decreases the number of resonant modes. Therefore, the consideration of realistic shear values also supports the hypothesis that only longer horizontal modes can propagate to the TIL.

It is obvious that one could extend linear approaches to two-layer and three-layer models including the stratosphere and the effect of the TIL (e.g., [Danielsen and Bleck 1970](#); [Gossard and Hooke 1975](#)). However, the resulting equations become complicated too and most of the time require numerical integration. Therefore, we now turn to the numerical integration of the full nonlinear equations [Eqs. (1)–(4)] as they allow a large number of tests to investigate the sensitivity of the solutions.

## 5. Numerical investigations

An extensive set of numerical simulations of the 3D flow above the Scandinavian mountains was performed to investigate the physical mechanisms leading to the very short trapped gravity waves within the TIL. It is shown that two properties of the background flow are essential and necessary for the generation of these short waves. First, it is the wind profile that allows vertically propagating mountain waves to

TABLE 3. Sensitivity experiment A: Impact of downward-propagating gravity waves. Here,  $\Delta x$ ,  $\Delta y$ , and  $\Delta z$  are the grid increments in the three spatial directions, and  $\Delta t$  is the time step. The values of  $n$ ,  $m$ , and  $l$  indicate the number of grid cells and  $nt$  indicates the number of time steps used in the integration. NPX and NPY are the number of processors for the horizontal domain decomposition in  $x$  and  $y$  directions used in the numerical integrations. The numbers epp0 and epp1 refer to the requested accuracy of the pressure solver at  $t = 0$ , and for the subsequent time steps, respectively, see Smolarkiewicz et al. (1997). The variable EXPER = 0 stands for the default numerical coding of the pressure solver. The variable  $D_{\text{abs}}$  denotes the vertical damping scale in Eq. (5). For all numerical simulations, upstream and ambient profiles are taken from T21 L137 as average from 1200 to 1800 UTC and taken at 61°N and 1°E (see Fig. 2).

Run	Varied parameters	Common parameters
Reference	$D_{\text{abs}} = 9.6 \text{ km}$	$\Delta x = \Delta y = 500 \text{ m}$ , $\Delta z = 250 \text{ m}$ , $\Delta t = 2 \text{ s}$ , $n = 2016$ , $m = 128$ , $l = 281$ , $nt = 43200$ Orography along 61°N NPX = 144, NPY = 8 EXPER = 0, epp0 = $10^{-6}$ , epp1 = $10^{-5}$ Compressible, no potential flow initialization
$D_{\text{abs}} = 12.8 \text{ km}$	$D_{\text{abs}} = 12.8 \text{ km}$	

break in the middle atmosphere. The strength of the low-level forcing and the presence of tropospheric and stratospheric jets are prerequisites to promote nonlinear instabilities and wave breaking in the negative shear zones above their cores, especially in regions where the magnitude of the wave-induced wind perturbations becomes comparable to the mean wind. Both the vertically propagating mountain waves and the wave-breaking regions modify the stratospheric airflow above the mountains compared to the upstream profiles. As a consequence, primary mountain waves that follow propagate into this modified airflow. In addition, the wave-breaking regions are secondary sources of short internal gravity waves. The second important component is the presence of large static stability  $N \geq 0.025 \text{ s}^{-1}$  within the TIL that exceed typical stratospheric values by 25% and more. To substantiate the

proposed mechanisms and to investigate the dependence of the wave response within the TIL on physical and numerical parameters, the 16 3D numerical simulations are grouped into physical and numerical sensitivity experiments.

a. Experiment A: Impact of downward-propagating gravity waves

The first sensitivity experiment A is dedicated to the question “Are downward-propagating gravity waves essential for the generation of horizontally short modes in the TIL?” To this end, two 3D simulations with different vertical profiles of imposed internal stratospheric friction are contrasted. Table 3 summarizes the setup of the numerical simulations. The reference simulation, using  $D_{\text{abs}} = 9.6 \text{ km}$  in Eq. (5), allows wave breaking in the middle atmosphere and contains downward-

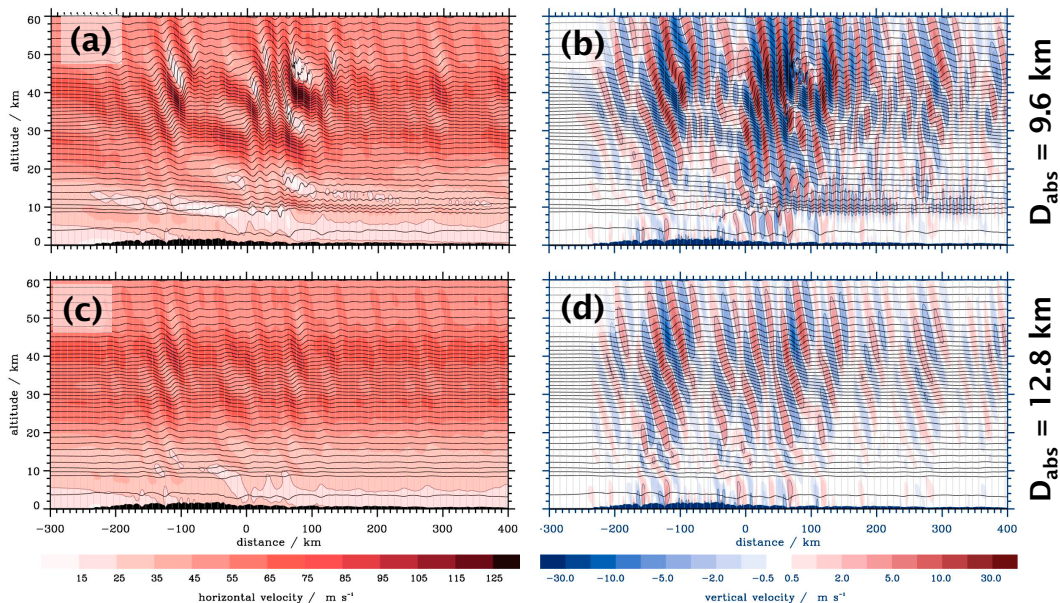


FIG. 9. (left) Horizontal and (right) vertical wind along the centerline  $y = 0$  of the 3D computational domain from (a),(b) the reference run and (c),(d) the run without wave breaking after 12-h simulation time. The black lines denote the potential temperature in logarithmic scaling, and the shaded area at the bottom of each panel is the orography. For the settings of the numerical parameters, refer to Table 3.

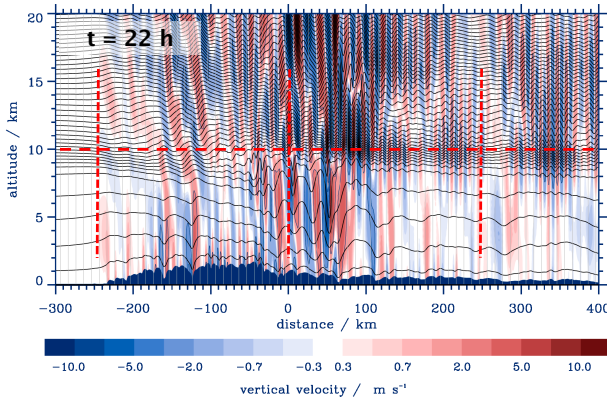


FIG. 10. Vertical wind along the centerline  $y = 0$  of the 3D computational domain from the reference run after 22-h simulation time. Thin black lines denote the potential temperature in logarithmic scaling, and the shaded area at the bottom is the orography. The horizontal red line denotes the altitude at which the Hovmöller plots are shown in Fig. 12. The vertical red lines denote the positions of the plots shown in Fig. 11. For the settings of the numerical parameters, refer to Table 3.

propagating modes. These modes are either reflected mountain waves or waves generated by secondary sources in the breaking region. The second simulation, using  $D_{abs} = 12.8$  km, keeps the amplitudes of the upward-propagating mountain waves finite and prevents wave breaking. As a result, only upward-propagating modes exist.

Figure 9 compares the results of the two numerical simulations. In the top row, the reference simulation shows the horizontal and vertical wind fields at the center line  $y = 0$

after 12-h simulation time. The atmospheric flow is dominated by upward-propagating mountain waves whose phase fronts are tilted into the wind. In addition, localized wave-breaking regions (i.e., overturning isentropes and strongly reduced horizontal wind) are visible above the TIL and in the stratosphere. In contrast, the simulation with enhanced stratospheric damping exclusively reveals upward-propagating mountain waves with no wave-breaking regions as shown in the lower row of Fig. 9. This simulation with the imposed finite-amplitude response does not yield short waves near the TIL.

Figure 10, showing the vertical wind from the reference simulation at 22 h, focuses on the shallow altitude region of interest, encompassing the troposphere and lower stratosphere up to 20-km altitude. With the adjusted color bar, the appearance of horizontally short waves over and downstream of the mountains becomes evident. Localized areas of wave breaking can be detected in the lower stratosphere. The short waves are trapped below the stratospheric wave-breaking region in a wave duct along the TIL.

The gradual formation of the stratospheric wave duct above and downstream of the mountains is demonstrated in Fig. 11 by showing the squared vertical wavenumber:

$$m^2 \approx \frac{N^2}{u^2} - \frac{1}{u} \frac{d^2 u}{dz^2} - k^2 (k = 2\pi/\lambda_x), \quad (8)$$

for stationary mountain waves (e.g., Achatz 2022, Eq. 7.76) with a horizontal wavelength  $\lambda_x = 12$  km. The small negative  $m^2$  values indicate that those waves are evanescent in the troposphere. A similar plot for  $\lambda_x = 15$  km (displace all curves in Fig. 11 to the right by  $0.15 \text{ km}^{-2}$ , which leads to positive but

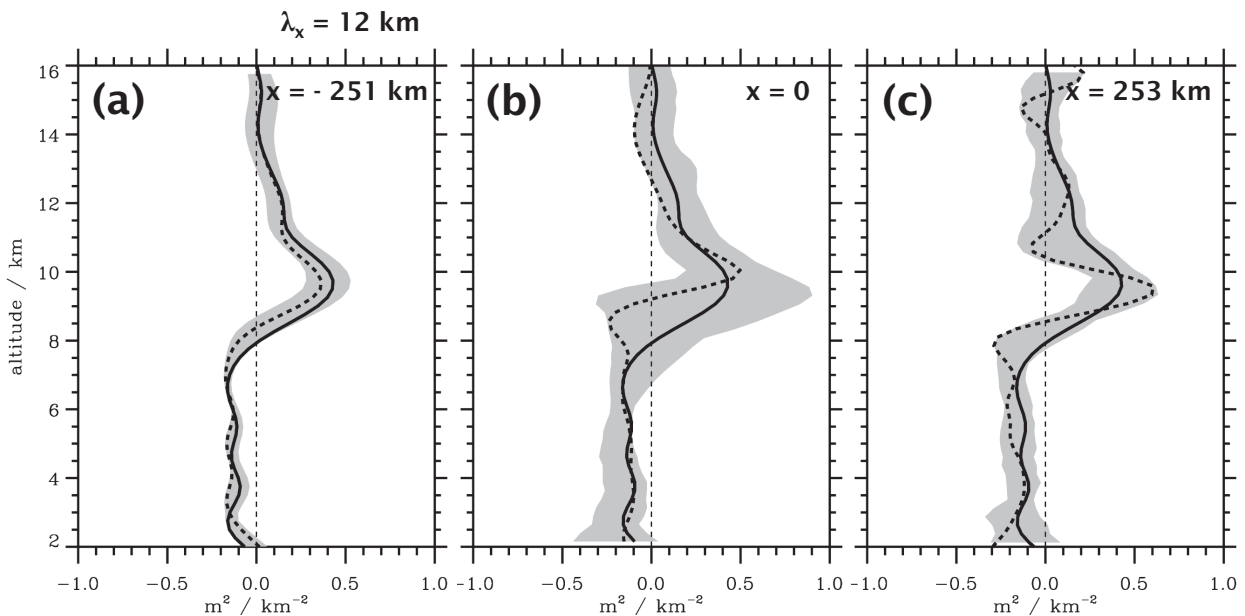


FIG. 11. Vertical  $m^2$  profiles for  $\lambda_x = 12$  km according to Eq. (8) at  $x$  positions along the centerline  $y = 0$  of the 3D computational domain from the reference run; see Fig. 10. Solid black line:  $t = 0$ , and dashed black line:  $t = 24$  h. The gray shaded area covers the temporal variability of the 1-min  $m^2$  profiles during the simulation.

small  $m^2$  values, i.e., long vertical wavelengths) explains the almost vertical phase lines of the simulated primary mountain waves with  $\lambda_x \geq 20$  km in the troposphere (Fig. 10). These numerical simulation results are consistent with the airborne DWL measurements over Scandinavia: Wagner et al. (2017) and Witschas et al. (2017) have demonstrated the existence of these trapped mountain waves with near-vertical phase lines throughout the troposphere caused by the flow over the underlying mountains.

In and above the TIL, the upstream  $m^2$  is positive and mountain waves with  $\lambda_x \geq 12$  km propagate freely (Fig. 11a). Above the mountains, the stratospheric wave breaking increases the variability of  $m^2$  near and above the TIL (Fig. 11b). Furthermore, the decreasing static stability  $N^2$  in the wave-breaking region at  $z > 10$  km leads to  $m^2$  falling to negative values in the course of the simulation (Fig. 11c). Simultaneously,  $N^2$  below 10 km is increased leading to larger positive  $m^2$  values. This vertically limited layer with  $m^2 > 0$  gradually forms the thermal wave duct in which the short gravity waves are trapped and propagate downstream. As mentioned above, Fig. 11 shows the profiles for  $\lambda_x = 12$  km, and a similar plot for  $\lambda_x = 15$  km only reveals a few instants when  $m^2 < 0$ . This means only short waves with  $\lambda_x \leq 12$  km can be guided along the wave duct.

Figure 10 is a snapshot taken from an animation of the entire numerical simulation over 24 h, which is provided by Dörnbrack (2024). When viewing this animation, both the formation of the stratospheric wave duct and the quasi-periodic vertical displacements of the tropopause due to the temporal modulation of strength and depth of the primary mountain waves, which lead to the temporal variability of  $m^2$ , become apparent (Fig. 11b). Wave packets with short horizontal wavelengths are emitted from this location and propagate downstream along the stratospheric wave duct.

Figure 12 displays the vertical velocity at 10-km altitude in the spirit of traditional Hovmöller plots. The comparison between the upper and lower panel of Fig. 12 reveals the distinct difference between the numerical simulations allowing/preventing stratospheric wave breaking: the finite-amplitude simulation produces steady mountain waves whose phase lines are stationary and which can be linked with the mountain ranges underneath (cf. Fig. 10). The flow response is completely different in the reference simulation, where the waves break in the stratosphere: temporal oscillations of the amplitude of the vertical wind appear in the phase lines associated with the main mountain ranges; see  $x < 100$  km or near  $x = 0$ . In addition, gravity waves with  $\lambda_x < 10$  km appear mostly in the lee of the mountains for  $x > 80$  km. The phase lines of these short modes propagate upstream, i.e., their ground-based phase speed is negative. However, groups of these short waves propagate downstream with a phase velocity of  $\sim 22$  m s<sup>-1</sup> as estimated from the dashed line in Fig. 12.

Figure 13 shows the vertical flux of wave energy  $EF_z$  at simulation times 12, 18, and 24 h. While the run without simulated wave breaking shows only positive, i.e., upward wave energy fluxes, the reference run shows regions (especially in the lower and middle stratosphere) where the wave energy propagates downward. At time  $t = 18$  h, it becomes apparent

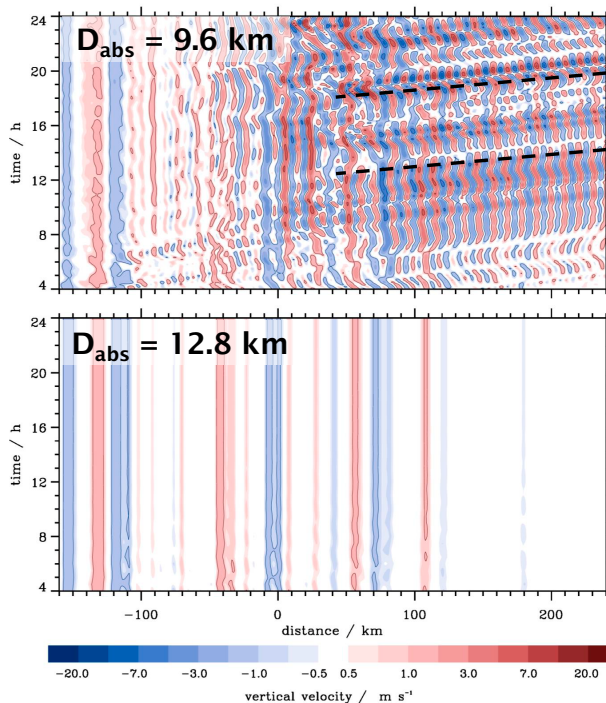


FIG. 12. Distance–time sections of the vertical wind component at 10-km altitude from (top) the reference run and (bottom) the run without wave breaking. For the numerical settings, see Table 3.

how  $EF_z$  oscillates between positive and negative values in the wave duct. This oscillation in the sign of  $EF_z$  is the signature of downstream-traveling wave packets. It must be noted that the regions with  $EF_z < 0$  extend up to  $\sim 20$ -km altitude, a fact that could explain the observed negative vertical energy fluxes at higher flight levels; see discussion in section 4c. In contrast, the finite amplitude simulation has already reached a quasi-steady state after 4 h, persisting until the end of the numerical integration at  $t = 24$  h as shown in the right column of Fig. 13. Obviously, the  $EF_z$  magnitudes of the finite-amplitude simulation are smaller due to the imposed damping according to Eq. (5). It should be noted that with longer filter lengths  $L = 50$  km, only a few, very sporadic downward-propagating waves occur in the reference run (not shown).

Figure 14 quantifies which spatial scales are involved in the different processes by presenting the binned power spectra of the vertical velocity and the vertical flux of the specific horizontal momentum  $u'w'$  at  $z = 5, 10,$  and  $20$  km, respectively. The temporally averaged vertical velocity energy spectra reveal power on horizontal scales from  $\sim 7$  to  $100$  km (top row in Fig. 14). Within the wave duct at 10-km altitude, the singular peak at  $\lambda_x \approx 10$  km occurs exclusively in the reference run. The run without wave breaking reveals a strongly attenuated response at  $\lambda_x \leq 30$  km, i.e., all short modes are absent here. It is important to note that the  $\lambda_x \approx 10$  km peak is neither present in the troposphere nor in the lower stratosphere. There, the amplitudes of the vertical wind become smaller and the energy shifts to longer horizontal modes (Fig. 14, top row).

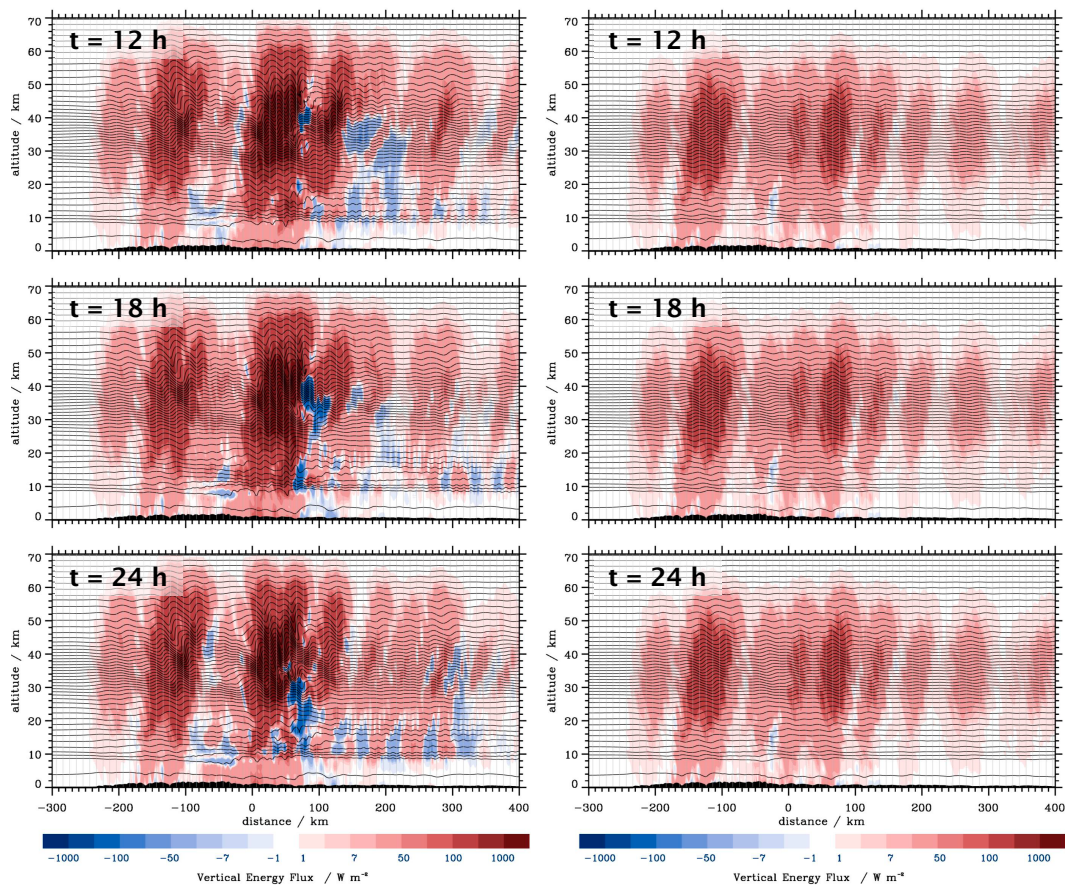


FIG. 13. Vertical energy fluxes  $EF_z$  after 12-, 18-, and 24-h simulation time for (left) the reference run and (right) the run without wave breaking. The  $EF_z$  is calculated with a 20-km smoothing window.

Gravity waves with  $\lambda_x < 10$  km along the wave duct do not transport horizontal momentum vertically upward, i.e., their momentum flux amplitudes are small, lower middle panel in Fig. 14. Positive and negative values at  $\lambda_x \approx 10$  km are associated with the upward- and downward-propagating modes as discussed before. Their time-averaged values are small compared to the specific momentum fluxes of the momentum-carrying waves at longer horizontal wavelengths  $\lambda_x > 20$  km. These are the upward-propagating mountain waves; see the bottom line of Fig. 14.

Figure 15 presents the binned power spectra at an altitude of 30 km to illustrate the excitation of short secondary modes due to wave breaking. The results of the selected wave-breaking periods (thin solid lines) are contrasted with the 12-h temporal averages (thick solid lines). Short modes with  $\lambda_x \lesssim 10$  km are visible for the vertical velocities (Fig. 15a). The coexistence of both positive and negative values of the specific momentum flux and the vertical wave energy flux indicates the power of these secondary gravity waves that propagate upward and downward (Figs. 15b and 15c). It is evident that the power of these short secondary waves is considerably lower than that of the longer, momentum-carrying waves in agreement with the 3D results of Woods and Smith (2011). It is therefore unlikely that these short

modes will reach the wave duct at 10 km given the downward increase in density. The negative horizontal wave energy flux for  $\lambda_x > 20$  km indicates the dominance of primary mountain waves that propagate upward and against the mean flow (Fig. 15d).

The conclusion from this physical sensitivity experiment A is as follows: Wave breaking modifies the stratospheric flow and the propagation conditions for the permanently excited primary mountain waves. In addition, the local body forces exerted by the breaking waves are a secondary source of gravity waves. However, it is the quasi-periodic modulation of the flow near the TIL and in the lower stratosphere that excites the short gravity waves. In the course of the numerical simulations, a thermal wave duct is formed, thereby strengthening the static stability of the TIL and favoring the occurrence of short trapped modes. These waves transport no horizontal momentum upward, they are transient, and they propagate in wave packets downstream.

#### b. Experiment B: Effects of orographic ruggedness

Although the results of the previous sections suggest that the short trapped waves are due to the interaction of the modified stratospheric airflow with the TIL and the downstream formation of a thermal wave duct, the following sensitivity

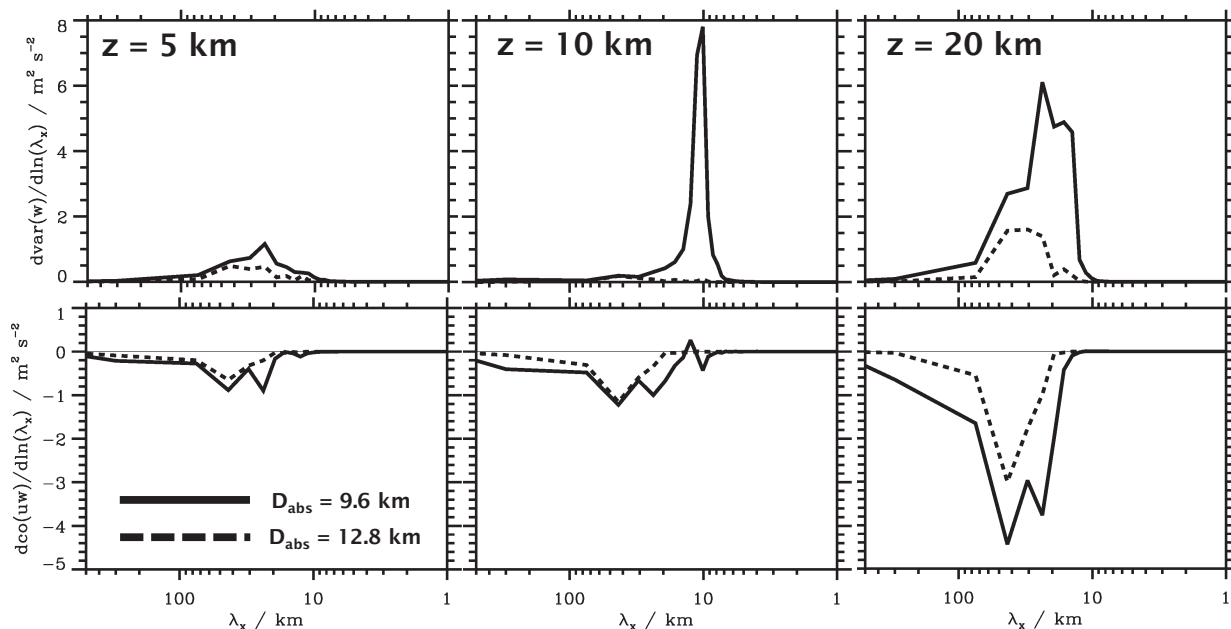


FIG. 14. (top) Binned power spectra of the vertical velocity and (bottom) the vertical flux of specific horizontal momentum  $u'w'$  at 5-, 10-, and 20-km altitude from the reference run (solid lines) and from the run without wave breaking (dashed lines) as temporal average from 12- to 24-h simulation time. For the numerical settings, see Table 3.

experiment B tests whether the rugged terrain could still be a source for the observed short waves. The orography  $z_{\text{ter}}$  at 61°N as shown by the black solid line in Fig. 16 depicts a compact landmass extending over nearly 650 km in west–east direction. There are deep notches and gaps in  $z_{\text{ter}}$  near the west coast of Norway. These steep orographic features result from the elongated and meandering Sognefjord. The cliffs around the Sognefjord rise almost vertically out of the water and reach heights of 1 km and more. The other curves in Fig. 16 present smoothed profiles filtered with boxcar average lengths of 10, 15, and 40 km, respectively. The left panel of Fig. 17 presents the binned power spectra of the four different orographic profiles. Indeed, the high-resolution orography without smoothing contains short modes between 5- and 20-km zonal wavelength. The smoothed curves increasingly lose spectral power in the small and longer modes.

The numerical simulations are summarized in Table 4. They are identical to the reference simulation of the previous subsection except that the numerical resolution has been increased by a factor of 2, i.e.,  $\Delta x = \Delta y = 250$  m, and the time step is  $\Delta t = 1$  s. The right panel of Fig. 17 shows the binned power spectra of the simulated vertical velocity at  $z = 10$  km altitude averaged from 12- to 24-h simulation time. A comparison of the amplitude of the power spectra here with that of the reference simulation in Fig. 14 shows that the increase in spectral power by around 50% is due to the increased numerical resolution.

However, the preservation of the spectral power for the smoothed terrain (10-km filter width; blue lines in Fig. 17) is the most important result of this sensitivity experiment B. If longer orographic modes are further attenuated by applying

greater boxcar average lengths, the momentum of the upward-propagating modes becomes too low to excite stratospheric wave breaking and the short waves along the wave duct disappear. Consequently, it is the primary upward-propagating mountain waves with  $\lambda_x \geq 20$  km that modify the stratospheric airflow leading to the trapped modes as described in section 5a.

### c. Experiment C: Impact of the TIL strength

An examination of Figs. 10 and 11c already reveals that the static stability along the TIL in the downstream segment is strongly increased due to the wave breaking in the lower stratosphere. For sensitivity experiment C, the vertical profile of the buoyancy frequency  $N(z)$  as computed from the upstream profiles (see Fig. 2c) is modified by adding a function  $f(z) = \Delta N \exp[-(z - z_{\text{TP}})^2 / \sigma_z^2]$  whereby  $z_{\text{TP}} = 9$  km and  $\sigma_z = 1.5$  km. The amplitude  $\Delta N$  is either  $0.010 \text{ s}^{-1}$  (red curve in Fig. 18) or  $0.015 \text{ s}^{-1}$  (blue curve in Fig. 18). From the modified  $N(z)$  profiles, the ambient  $\theta_e$  profiles are computed numerically. Other parameters of the numerical setting are provided in Table 5.

Figure 19 demonstrates the impact of increasing the upstream TIL strength on the short-wave response. The common feature of the sensitivity experiment C is that a stronger TIL (higher peak  $N$  value) leads to shorter gravity waves within the TIL. Figure 19 also demonstrates another interesting finding in comparison to the measured amplitudes of the trapped waves during the DLR Falcon flights along legs RF07-FL2 and RF08-FL1: The amplitude of the numerically produced waves now compares quantitatively very well with the observations. Furthermore, the wave response at 12-km altitude

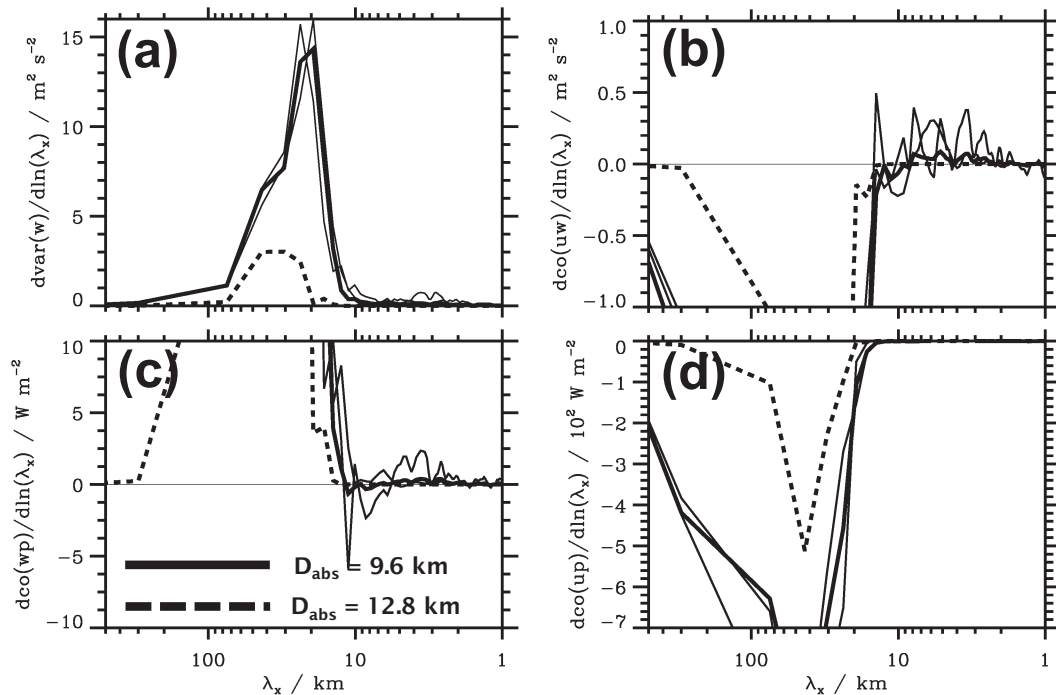


FIG. 15. (a) Binned power spectra of the vertical velocity, (b) the vertical flux of specific horizontal momentum, and (c) the vertical and the zonal fluxes of wave energy, (d) at 30-km altitude from the reference run (thick solid lines) and from the run without wave breaking (thick dashed lines) as temporal average from 12- to 24-h simulation time. The thin black lines are the spectra averaged over 2-h periods beginning at 12.5- and 15.5-h simulation time, respectively. For the numerical settings, see Table 3.

is still large and agrees well with the HALO observations along track HL3 (right panel in Fig. 19).

#### d. Experiment D: Impact of numerical settings

Eight further numerical simulations form the final sensitivity experiment D that investigates the dependence of the solutions on selected numerical settings. The parameters of the different runs are summarized in Table 6. Figure 20 groups

the results of this sensitivity experiment in three panels, which in turn show the binned power spectra of the simulated vertical velocity at an altitude of 10 km. The black solid line, which can be seen in all panels, is the reference run attaining a spectral amplitude of  $7 \text{ m}^2 \text{ s}^{-2}$  at  $\lambda_x \approx 10 \text{ km}$ .

Initially, the numerical integrations were modified to a potential flow initialization (red curve in Fig. 20a) and to an integration of the anelastic equations (Smolarkiewicz and

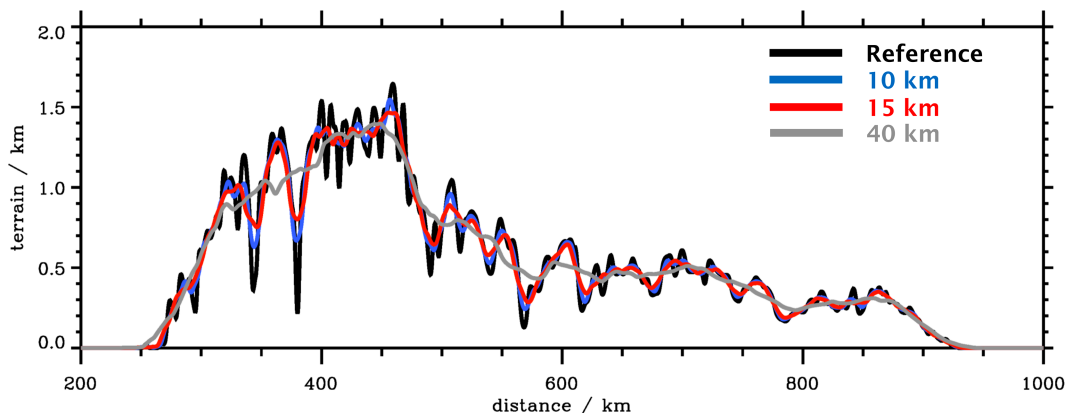


FIG. 16. Profiles of the digital orographies used for the sensitivity experiment B. The black line marks the orography along  $61^\circ\text{N}$  interpolated to a 250-m grid and smoothed over three grid points as used for the reference run. The numbers on the colored lines denote the boxcar average lengths used to smooth the orography.



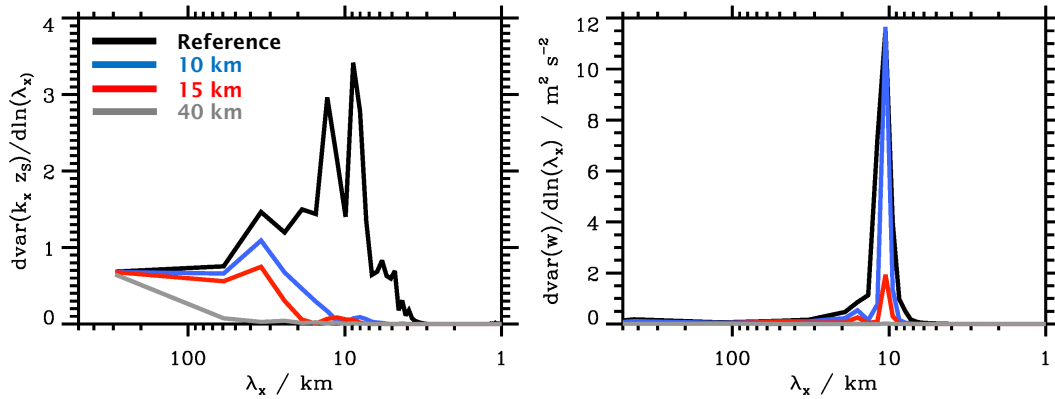


FIG. 17. (left) Binned power spectra of the digital orographies used for the sensitivity experiment B. (right) Binned power spectra of the vertical velocity at  $z = 10$  km altitude. The reference run, here, refers to the same numerical settings as presented before but with the increased spatial resolution of  $\Delta x = \Delta y = 250$  m. For the numerical settings, see Table 4. Same line coding as in Fig. 16.

Dörnbrack 2008) (blue curve in Fig. 20a). Both model options increase the spectral amplitude by either 8% or 29%. Thus, the chosen numerical initialization has almost no effect of the amplitude of the trapped waves. The small difference between the integration of the fully compressible equations and the sound-proofed equation confirms former numerical (Smolarkiewicz and Dörnbrack 2008) and theoretical findings (Klein et al. 2010). It must be noted that the run time is only 42% for the anelastic integration compared to the integration of the compressible equations.

The second group of numerical simulations concerns the accuracy of the iterative pressure solver. The variables `epp0` and `epp1` in Fig. 20b and Table 6 refer to the dimensionless norm of the divergence residual and denote how accurately the flow field is made divergence free (Smolarkiewicz et al. 1997, Eq. 4). Two different stopping criteria are applied for the first time step (`epp0`) and for all other ones (`epp1`). The accuracy of the pressure solver has a marginal effect on the spectral amplitude (increase by  $\sim 12\%$ ). Likewise, another option to optimize the performance of pressure solver (`EXPER = 3`) reduces the spectral amplitude just by 7% (Figure 20b). Indeed, with this optimization, the runtime is only 82% compared to the reference run.

Figure 20(c) presents the results for simulations using a different domain decomposition of EULAG, i.e., different number of processors in the horizontal directions. In addition, a compiler statement for vectorization was activated, which was not used in all other runs. The spectral amplitudes vary by only  $\pm 15\%$ . For the run with  $288 \times 16$  processors, the runtime is reduced to 1/3; for the run with  $96 \times 4$  processors, the runtime increases by a factor of 2.75.

All numerical changes in the settings have only a marginal impact on the spectral amplitude of the vertical wind component at an altitude of 10 km. The presented numbers must be related to the almost complete extinction of the short waves (amplitude reduction to 2%) using the stratospheric damping as presented in Fig. 14 of section 5a.

### 6. Discussion and conclusions

Gravity waves with  $\lambda_x \leq 10$  km were observed during two research flights within the TIL over southern Scandinavia; see Gisinger et al. (2020), Witschas et al. (2023) and Figs. 4 and 5. The DLR Falcon observations indicate that these short gravity waves are most likely nonstationary (section 4d). The estimated vertical fluxes of wave energy and horizontal momentum are

TABLE 4. Sensitivity experiment B: effects of orographic rugeness. The names in the first column refer to the line legends in Fig. 17. Refer to Table 3 for explanation of the used parameter names. For all numerical simulations, upstream and ambient profiles are taken from T21 L137 as average from 1200 to 1800 UTC and taken at 61°N and 1°E (see Fig. 2).

Run	Varied parameters	Common parameters
Reference (high)	$z_{\text{ter}}$ unfiltered	$\Delta x = \Delta y = \Delta z = 250$ m, $\Delta t = 1$ s, $n = 4032$ , $m = 256$ , $l = 281$ , $nt = 86\,400$ Orography along 61°N $D_{\text{abs}} = 9.6$ km NPX = 288, NPY = 16 EXPER = 0, $epp0 = 10^{-6}$ , $epp1 = 10^{-5}$ Compressible, no potential flow initialization
10 km	$z_{\text{ter}}$ with boxcar length = 10 km	
15 km	$z_{\text{ter}}$ with boxcar length = 15 km	
40 km	$z_{\text{ter}}$ with boxcar length = 40 km	

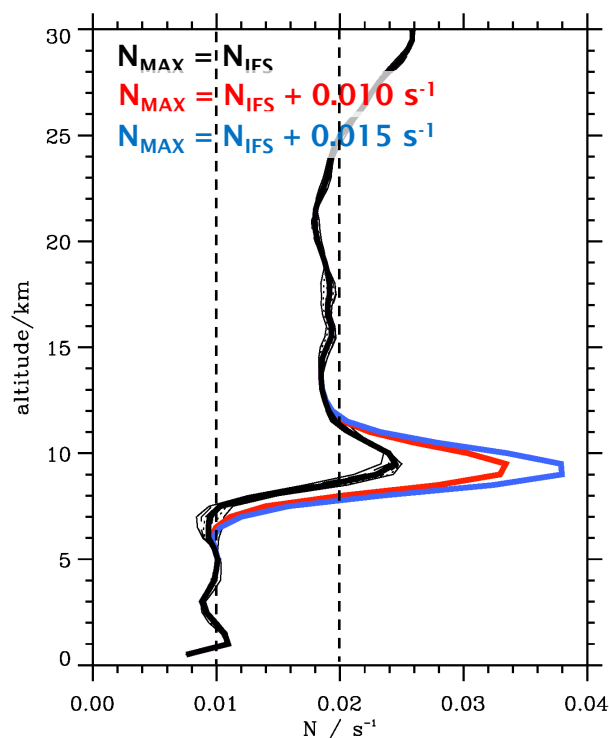


FIG. 18. Vertical profiles of the buoyancy frequency  $N$  as used for the sensitivity experiment C with varying values of the strength of the TIL. The  $N$  profiles are used to compute the background potential temperature profiles  $\Theta_e(z)$ .

small compared to other cases observed over the Sierra Nevada during T-REX (Smith et al. 2008), over the Southern Alps during DEEPWAVE (Smith et al. 2016), and also over the Southern Andes during SOUTHTRAC (Dörnbrack et al. 2022a). The smallness of the vertical flux of horizontal momentum is due to the predominance of internal gravity waves with  $\lambda_x \lesssim 10$  km trapped within the stratospheric wave duct along the TIL.

Similar airborne observations were reported earlier from the T-REX field campaign over the Sierra Nevada (Smith et al. 2008; Woods and Smith 2010, 2011). Woods and Smith

(2011) interpreted their occurrence as indirect evidence of downgoing secondary waves generated by stratospheric wave breaking aloft. Their idealized numerical simulations of the flow across a smooth bell-shaped mountain and using midlatitude climatological winter profiles of wind and thermal stability at 40° and 50°N supported their hypothesis (Woods and Smith 2011).

Here, the Scandinavian observations at 61°N are investigated by conducting three-dimensional numerical simulations using upstream wind and stability profiles from the time of the observations as initial and background conditions. At the lower boundary, a realistic high-resolution orography is specified. Another distinctive feature of the present case compared to Woods and Smith (2011) is the presence of a pronounced TIL, a sharp inversion layer capping the troposphere under the nearly steady high pressure ridge during the time of the observations.

The most important of the four numerical sensitivity experiments demonstrates that mountain-wave breaking in the middle atmosphere and the subsequent modification of the stratospheric flow above the TIL are indeed the key factors for the occurrence of short trapped modes along the TIL (section 5a). In particular, and in contrast to the results of Woods and Smith (2011), a thermal wave duct gradually forms underneath the lower stratospheric wave-breaking region as the numerical simulation progresses. When stratospheric breaking of the primary mountain waves is intentionally suppressed by adding additional viscosity to the numerical integration, the simulated atmospheric flow remains steady, and the short waves along the TIL are absent (section 5a).

Simulated mountain waves transporting horizontal momentum are in the range of  $\lambda_x \approx 20$ –30 km in accordance with the results from T-REX (Smith et al. 2008) and DEEPWAVE (Smith and Kruse 2017). These waves propagate through the troposphere entering the stratosphere and mesosphere. In the middle atmosphere, these vertically propagating mountain waves become convectively unstable. The associated local deceleration may reflect primary mountain waves. Furthermore, the stratospheric airflow above the mountain range is modified into which subsequent mountain waves propagate. The momentum deposition by the breaking mountain waves is also a local body force that represents a secondary source of

TABLE 5. Sensitivity experiments C: Impact of the TIL strength. The function  $f(z) = \exp\{-(z - z_{TP})^2/\sigma_z^2\}$  describes the modification of the TIL whereby  $z_{TP} = 9$  km and  $\sigma_z = 1.5$  km. The vertical profiles of the buoyancy frequencies  $N(z)$  are shown in Fig. 18. For all numerical simulations, upstream and ambient profiles are taken from T21 L137 as average from 1200 to 1800 UTC and taken at 61°N and 1°E (see Fig. 2).

Run	Varied parameters	Common parameters
Reference (high)	$N_{\text{IFS}}(z)$	$\Delta x = \Delta y = \Delta z = 250$ m, $\Delta t = 1$ s, $n = 4032$ , $m = 256$ , $l = 281$ , $nt = 86\,400$ Orography along 61°N $D_{\text{abs}} = 9.6$ km NPX = 288, NPY = 16 EXPER = 0, epp0 = $10^{-6}$ , epp1 = $10^{-5}$ Compressible, no potential flow initialization
	$N_{\text{IFS}}(z) + 0.010f(z) \text{ s}^{-1}$	
	$N_{\text{IFS}}(z) + 0.015f(z) \text{ s}^{-1}$	

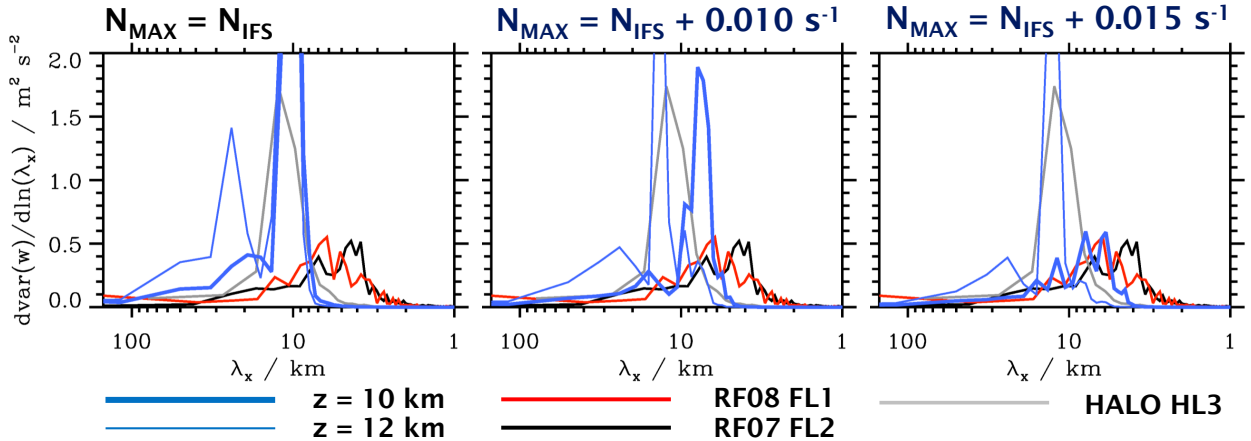


FIG. 19. Sensitivity of the binned vertical variance spectra within the wave duct as function of TIL strength. The simulation results are shown at 10- and 12-km altitude as temporal averages from 9- to 15-h simulation time. For the numerical settings, see Table 5. The airborne observations from flight legs RF07-FL2, RF08-FL01, and HL3 are superimposed (cf. Fig. 6).

gravity waves (e.g., Dong et al. 2022). In agreement with the 3D numerical simulation results of Woods and Smith (2011), their energy and momentum fluxes are very small. Therefore, it is unlikely that these secondary gravity waves cause the trapped short waves, as their low amplitudes at source level will certainly be further attenuated as they propagate downward toward the TIL. It is the formation of the stratospheric wave duct and its persistent disturbances by oscillating mountain waves that causes the short waves to be trapped along the TIL.

A further sensitivity experiment varied the orographic ruggedness (section 5b) by smoothing the high-resolution terrain. Only if filter lengths larger than 10 km are applied, the momentum of the upward-propagating modes  $\lambda_x \geq 20$  km becomes too low to excite stratospheric wave breaking and the short waves at the TIL disappear. This finding that the short modes with  $\lambda_x \leq 10$  km are not directly caused by the rugged terrain is supported by linear wave theory using uniform or sheared wind profiles (section 4d). The variation of different

physical and numerical parameters reveals that their horizontal wavelength is mainly influenced by the sharpness of the tropopause, i.e., the strength of the TIL. The stronger the TIL, i.e., the larger the local value of  $N(z)$ , the shorter the simulated waves (section 5c). Interestingly, as an aside, an increase in the buoyancy frequency  $N(z)$  in the TIL of the upstream profiles leads to a satisfactory quantitative agreement with the airborne measurements. This finding points to the potential unreliability of the  $N(z)$  profiles computed from the IFS operational analyses, which only have  $\sim 300$ -m vertical resolution around this altitude. Increasing the spatial resolution increases the spectral power of the trapped waves by about 50% (section 5b). Other parameters like the settings of the numerical solver impact the results less (section 5d).

Finally, it should be added that great care should be taken when choosing the height of the model top. The presented numerical simulations indicate that computational domains encompassing the troposphere and the stratosphere/mesosphere

TABLE 6. Sensitivity experiment D: Impact of numerical settings. Parameters that are varied are in bold, and all other parameters remain the same as in the reference run. The names in the first column refer to the line legends in Fig. 20. For all numerical simulations, upstream and ambient profiles are taken from T21 L137 as average from 1200 to 1800 UTC and taken at 61°N and 1°E; see Fig. 2. Refer to Table 3 for explanation of the used parameter names.

Run	Varied parameters	Common parameters
Reference	NPX = 144, NPY = 8 EXPER = 0, epp0 = $10^{-6}$ , epp1 = $10^{-5}$ Compressible, no potential flow initialization	$\Delta x = \Delta y = 500$ m, $\Delta z = 250$ m, $\Delta t = 2$ s $n = 2016$ , $m = 128$ , $l = 281$ , $nt = 43200$ $D_{\text{abs}} = 9.6$ km
Potential flow	<b>Potential flow initialization</b>	
Anelastic	<b>Integration of the anelastic equations</b>	
EXPER = 3	<b>Memory-efficient coding of the pressure solver</b>	
epp1 = $10^{-3}$	<b>epp0 = <math>10^{-4}</math>, epp1 = <math>10^{-3}</math></b>	
epp1 = $10^{-7}$	<b>epp0 = <math>10^{-8}</math>, epp1 = <math>10^{-7}</math></b>	
NPX = 288, NPY = 16	<b>NPX = 288, NPY = 16</b>	
NPX = 96, NPY = 4	<b>NPX = 96, NPY = 4</b>	
Vector compiler	<b>-xCORE-AVX512</b>	

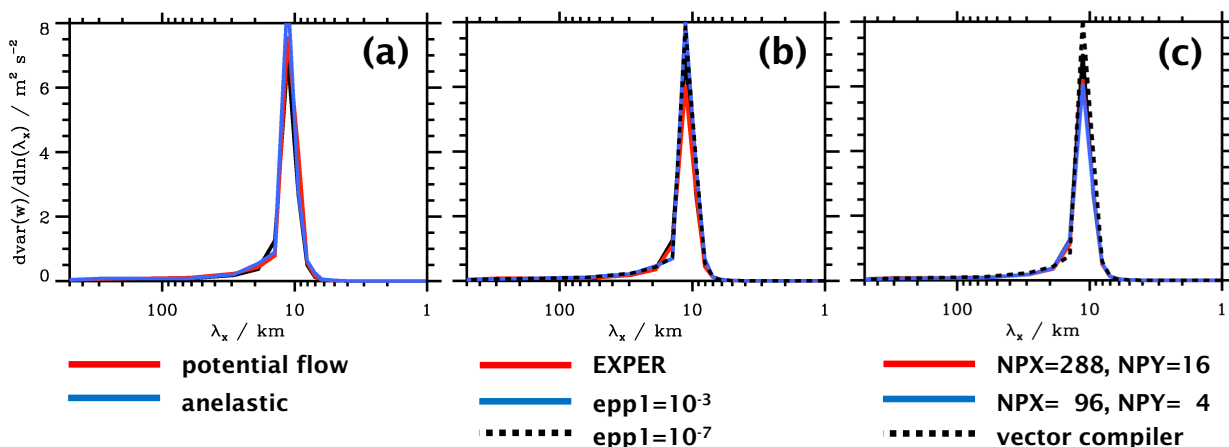


FIG. 20. Sensitivity of the binned vertical variance spectra within the wave duct as a function of numerical settings; for details, see Table 6. Results are shown at 10-km altitude as temporal averages from 12- to 24-h simulation time. In all panels, the black lines (which are normally overlaid by the other lines) refer to the reference run.

are essential to properly simulate the fine-scale and transient dynamics at the tropopause.

*Acknowledgments.* This work was partly funded by the Federal Ministry for Education and Research under Grant 01LG1907 (Project WASCLIM) in the frame of the Role of the Middle Atmosphere in Climate (ROMIC) program. Further support by the German Science foundation under Grants GW-TP/DO 1020/9-1 and PACOG/RA 1400/6-1 in the frame of the DFG-research group MS-GWAVES is also acknowledged. Access to the operational ECMWF data used for the interpolation onto the HALO flight tracks was granted through the special project “Gravity Waves and Turbulence over the Andes.” The numerical simulations were conducted at the German Climate Computing Center (Deutsches Klimarechenzentrum, DKRZ) and the Leibniz Supercomputing Centre (LRZ; <https://www.lrz.de>). The author gratefully acknowledges the Gauss Centre for Supercomputing e.V. (<https://www.gauss-centre.eu>) for providing computing time on the GCS Supercomputer SuperMUC LRZ. The author thanks Piotr K. Smolarkiewicz for reading an early version of the paper and the stimulating discussions. The author is also grateful for the continued interest of the reviewers Dave Fritts and Ulrich Achatz and would like to thank a third anonymous referee.

*Data availability statement.* The in situ airborne observations are available from the HALO database at <https://halo-db.pa.op.dlr.de>. The in situ data from the DLR Falcon data have the dataset numbers 4366 and 4367, and the BAHAMAS data from HALO have the number 3837. The DWL data can be accessed via the dataset numbers 4394 and 4395. The ECMWF IFS data interpolated along the aircraft’s flight tracks have the dataset number 5828. The operational analyses of the ECMWF are publicly available via their website at <https://www.ecmwf.int>. Due to the large magnitude of the binary data from the numerical EULAG runs, these data are available on request.

## APPENDIX

### Airborne Observations

The airborne in situ observations were conducted on the DLR Falcon and the HALO research aircraft by means of a nose boom probe with a 5-hole sensor. The in situ observations collected by the Basic HALO Measurement and Sensor System (BAHAMAS) provide high-resolution measurements of

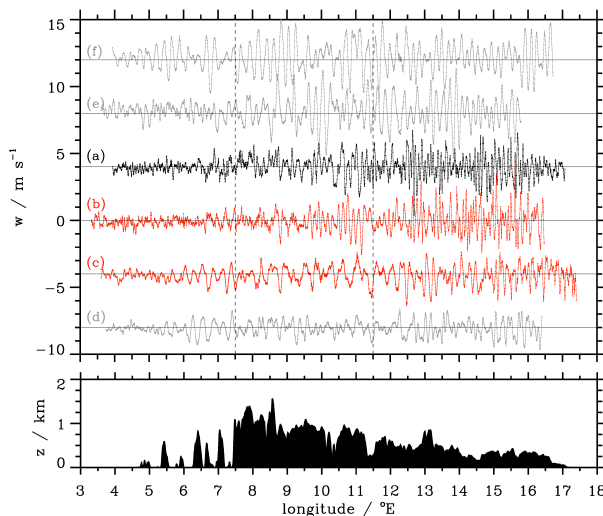


FIG. A1. Vertical velocity along the six cross mountain legs of the research flights of DLR Falcon and HALO. (a) RF07-FL2, (b) RF08-FL1, (c) HL1, (d) HL2, (e) HL3, and (f) HL4. The red lines (b) and (c) mark simultaneous measurements at vertically staggered legs, the lines (c) and (d) are nearly simultaneous HALO measurements (about 10-min difference at the western way point, about 1-h time lag at the eastern end), and the gray lines (e) and (f) mark the upper-level legs of HALO. The line colors correspond to the ones used in Table 1 and Fig. 4. The vertical dashed lines mark the boundaries between the upstream, ridge, and downstream segments.

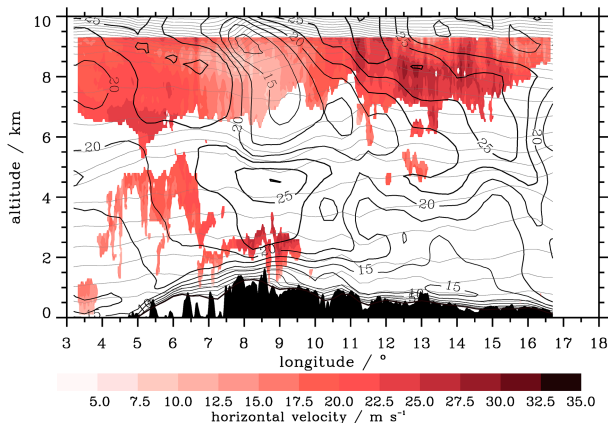


FIG. A2. Magnitude of the horizontal wind ( $\text{m s}^{-1}$ ; color shaded; forward-backward scanning DWL; 5-s resolution data smoothed with a 10-s filter), IFS potential temperature (K; gray contour lines; 2-K intervals), and horizontal wind ( $\text{m s}^{-1}$ ; black contour lines) interpolated along the flight track RF08-FL1. ASTER orography underneath the flight path in black. The bold black line marks the IFS orography.

horizontal and vertical wind components as well as temperatures, pressures, and water vapor mixing ratios at flight altitude with high temporal resolution, i.e., up to 100 Hz (Giez et al. 2017, 2019, 2021, 2022). Details to the in situ measurements and remote sensing DWL observations on board the DLR Falcon including information on the accuracy and precision can be found in Gisinger et al. (2020) and Witschas et al. (2023). Figure A1 displays the airborne in situ measurements of the vertical wind on board the DLR Falcon and the German research aircraft HALO during along the six cross-mountain legs; see Table 1 for the details of times and altitudes. Figures 5 and A2 display the DWL measurements along the two cross-mountain legs of the DLR Falcon. In addition to previous visualizations by Gisinger et al. (2020) or by Witschas et al. (2023), contour lines of the potential temperature and the horizontal wind from interpolated IFS fields are superimposed.

## REFERENCES

- Achatz, U., 2022: *Atmospheric Dynamics*. 1st ed. Springer, 554 pp., <https://doi.org/10.1007/978-3-662-63941-2>.
- Birner, T., A. Dörnbrack, and U. Schumann, 2002: How sharp is the tropopause at midlatitudes? *Geophys. Res. Lett.*, **29**, 1700, <https://doi.org/10.1029/2002GL015142>.
- Bramberger, M., and Coauthors, 2017: Does strong tropospheric forcing cause large-amplitude mesospheric gravity waves? A DEEPWAVE case study. *J. Geophys. Res. Atmos.*, **122**, 11 422–11 443, <https://doi.org/10.1002/2017JD027371>.
- Danielsen, E. F., and R. Bleck, 1970: Tropospheric and stratospheric ducting of stationary mountain lee waves. *J. Atmos. Sci.*, **27**, 758–772, [https://doi.org/10.1175/1520-0469\(1970\)027<0758:TASDOS>2.0.CO;2](https://doi.org/10.1175/1520-0469(1970)027<0758:TASDOS>2.0.CO;2).
- Dong, W., D. C. Fritts, M. P. Hickey, A. Z. Liu, T. S. Lund, S. Zhang, Y. Yan, and F. Yang, 2022: Modeling studies of gravity wave dynamics in highly structured environments: Reflection, trapping, instability, momentum transport, secondary gravity waves, and induced flow responses. *J. Geophys. Res. Atmos.*, **127**, e2021JD035894, <https://doi.org/10.1029/2021JD035894>.
- Dörnbrack, A., 2024: Vertical velocity and potential temperature of the flow across the Scandinavian mountains. Zenodo, accessed 29 August 2024, <https://doi.org/10.5281/zenodo.10718945>.
- , T. Birner, A. Fix, H. Flentje, A. Meister, H. Schmid, E. V. Browell, and M. J. Mahoney, 2002: Evidence for inertia gravity waves forming polar stratospheric clouds over Scandinavia. *J. Geophys. Res.*, **107**, 8287, <https://doi.org/10.1029/2001JD000452>.
- , P. Bechtold, and U. Schumann, 2022a: High-resolution aircraft observations of turbulence and waves in the free atmosphere and comparison with global model predictions. *J. Geophys. Res. Atmos.*, **127**, e2022JD036654, <https://doi.org/10.1029/2022JD036654>.
- , S. D. Eckermann, B. P. Williams, and J. Haggerty, 2022b: Stratospheric gravity waves excited by a propagating Rossby wave train—A DEEPWAVE case study. *J. Atmos. Sci.*, **79**, 567–591, <https://doi.org/10.1175/JAS-D-21-0057.1>.
- Durrán, D. R., 1990: Mountain waves and downslope winds. *Atmospheric Processes over Complex Terrain*, W. Blumen, Ed., American Meteorological Society, 59–81, [https://doi.org/10.1007/978-1-935704-25-6\\_4](https://doi.org/10.1007/978-1-935704-25-6_4).
- Dutton, J. A., 1976: *The Ceaseless Wind*. 1st ed. McGraw-Hill, 579 pp.
- Eliassen, A., and E. Palm, 1961: On the transfer of energy in stationary mountain waves. *Geophys. Publ.*, **22** (3), 1–23.
- Fritts, D. C., and M. J. Alexander, 2003: Gravity wave dynamics and effects in the middle atmosphere. *Rev. Geophys.*, **41**, 1003, <https://doi.org/10.1029/2001RG000106>.
- , and Coauthors, 2016: The Deep Propagating Gravity Wave Experiment (DEEPWAVE): An airborne and ground-based exploration of gravity wave propagation and effects from their sources throughout the lower and middle atmosphere. *Bull. Amer. Meteor. Soc.*, **97**, 425–453, <https://doi.org/10.1175/BAMS-D-14-00269.1>.
- , W. Dong, T. S. Lund, S. Wieland, and B. Laughman, 2020: Self-acceleration and instability of gravity wave packets: 3. Three-dimensional packet propagation, secondary gravity waves, momentum transport, and transient mean forcing in tidal winds. *J. Geophys. Res. Atmos.*, **125**, e2019JD030692, <https://doi.org/10.1029/2019JD030692>.
- Giez, A., C. Mallaun, M. Zöger, A. Dörnbrack, and U. Schumann, 2017: Static pressure from aircraft trailing-cone measurements and numerical weather-prediction analysis. *J. Aircr.*, **54**, 1728–1737, <https://doi.org/10.2514/1.C034084>.
- , M. Zöger, V. Dreiling, and C. Mallaun, 2019: Static source error calibration of a nose boom mounted air data system on an atmospheric research aircraft using the trailing cone method. DLR Tech. Rep. 2019-07, 87 pp., <https://elib.dlr.de/135789/>.
- , C. Mallaun, V. Nenakhov, and M. Zöger, 2021: Calibration of a nose boom mounted airflow sensor on an atmospheric research aircraft by inflight maneuvers. DLR Tech. Rep. 2021-17, 179 pp., <https://elib.dlr.de/145704/>.
- , M. Zöger, C. Mallaun, V. Nenakhov, M. Schimpf, C. Grad, A. Numberger, and K. Raynor, 2022: Determination of the measurement errors for the HALO basic data system BAHAMAS by means of error propagation. DLR Tech. Rep. 2022-27, 97 pp., <https://doi.org/10.57676/5rdc-q708>.
- Gisinger, S., J. Wagner, and B. Witschas, 2020: Airborne measurements and large-eddy simulations of small-scale gravity waves at the tropopause inversion layer over Scandinavia. *Atmos. Chem. Phys.*, **20**, 10 091–10 109, <https://doi.org/10.5194/acp-20-10091-2020>.
- Gossard, E. E., and W. H. Hooke, 1975: *Waves in the Atmosphere: Atmospheric Infrasound and Gravity Waves: Their Generation*

- and Propagation. Development in Atmospheric Science, Vol. 2, Elsevier Scientific Publishing Company, 456 pp.
- Grubišić, V., and Coauthors, 2008: The terrain-induced rotor experiment: A field campaign overview including observational highlights. *Bull. Amer. Meteor. Soc.*, **89**, 1513–1534, <https://doi.org/10.1175/2008BAMS2487.1>.
- Hersbach, H., and Coauthors, 2020: The ERA5 global reanalysis. *Quart. J. Roy. Meteor. Soc.*, **146**, 1999–2049, <https://doi.org/10.1002/qj.3803>.
- Hólm, E., R. Forbes, S. Lang, L. Magnusson, and S. Malardel, 2016: New model cycle brings higher resolution. *ECMWF Newsletter*, No. 147, ECMWF, Reading, United Kingdom, 14–19, <https://www.ecmwf.int/sites/default/files/elibrary/2016/16299-newsletter-no147-spring-2016.pdf>.
- Isler, J. R., M. J. Taylor, and D. C. Fritts, 1997: Observational evidence of wave ducting and evanescence in the mesosphere. *J. Geophys. Res.*, **102**, 26301–26313, <https://doi.org/10.1029/97JD01783>.
- Klein, R., U. Achatz, D. Bresch, O. M. Knio, and P. K. Smolarkiewicz, 2010: Regime of validity of soundproof atmospheric flow models. *J. Atmos. Sci.*, **67**, 3226–3237, <https://doi.org/10.1175/2010JAS3490.1>.
- Krisch, I., M. Ern, L. Hoffmann, P. Preusse, C. Strube, J. Ungermann, W. Woiwode, and M. Riese, 2020: Superposition of gravity waves with different propagation characteristics observed by airborne and space-borne infrared sounders. *Atmos. Chem. Phys.*, **20**, 11469–11490, <https://doi.org/10.5194/acp-20-11469-2020>.
- Prusa, J. M., P. K. Smolarkiewicz, and R. R. Garcia, 1996: Propagation and breaking at high altitudes of gravity waves excited by tropospheric forcing. *J. Atmos. Sci.*, **53**, 2186–2216, [https://doi.org/10.1175/1520-0469\(1996\)053<2186:PABAHA>2.0.CO;2](https://doi.org/10.1175/1520-0469(1996)053<2186:PABAHA>2.0.CO;2).
- , —, and A. A. Wyszogrodzki, 2008: EULAG, a computational model for multiscale flows. *Comput. Fluids*, **37**, 1193–1207, <https://doi.org/10.1016/j.compfluid.2007.12.001>.
- Queney, P., G. A. Corby, N. Gerbier, H. Koschmieder, and J. Zierep, 1960: Part II – A survey of theoretical studies. The airflow over mountains. WMO Tech. Note WMO-98.TP.34, 49–107.
- Satomura, T., and K. Sato, 1999: Secondary generation of gravity waves associated with the breaking of mountain waves. *J. Atmos. Sci.*, **56**, 3847–3858, [https://doi.org/10.1175/1520-0469\(1999\)056<3847:SGOGWA>2.0.CO;2](https://doi.org/10.1175/1520-0469(1999)056<3847:SGOGWA>2.0.CO;2).
- Schoeberl, M. R., 1985: The penetration of mountain waves into the middle atmosphere. *J. Atmos. Sci.*, **42**, 2856–2864, [https://doi.org/10.1175/1520-0469\(1985\)042<2856:TPOMWI>2.0.CO;2](https://doi.org/10.1175/1520-0469(1985)042<2856:TPOMWI>2.0.CO;2).
- Smith, R. B., and C. G. Kruse, 2017: Broad-spectrum mountain waves. *J. Atmos. Sci.*, **74**, 1381–1402, <https://doi.org/10.1175/JAS-D-16-0297.1>.
- , B. K. Woods, J. Jensen, W. A. Cooper, J. D. Doyle, Q. Jiang, and V. Grubišić, 2008: Mountain waves entering the stratosphere. *J. Atmos. Sci.*, **65**, 2543–2562, <https://doi.org/10.1175/2007JAS2598.1>.
- , and Coauthors, 2016: Stratospheric gravity wave fluxes and scales during DEEPWAVE. *J. Atmos. Sci.*, **73**, 2851–2869, <https://doi.org/10.1175/JAS-D-15-0324.1>.
- Smolarkiewicz, P. K., and L. G. Margolin, 1997: On forward-in-time differencing for fluids: An Eulerian/semi-Lagrangian non-hydrostatic model for stratified flows. *Atmos.–Ocean*, **35**, 127–152, <https://doi.org/10.1080/07055900.1997.9687345>.
- , and A. Dörnbrack, 2008: Conservative integrals of adiabatic Durran's equations. *Int. J. Numer. Methods Fluids*, **56**, 1513–1519, <https://doi.org/10.1002/fld.1601>.
- , V. Grubišić, and L. G. Margolin, 1997: On forward-in-time differencing for fluids: Stopping criteria for iterative solutions of anelastic pressure equations. *Mon. Wea. Rev.*, **125**, 647–654, [https://doi.org/10.1175/1520-0493\(1997\)125<0647:OFITDF>2.0.CO;2](https://doi.org/10.1175/1520-0493(1997)125<0647:OFITDF>2.0.CO;2).
- , C. Kühnlein, and N. P. Wedi, 2014: A consistent framework for discrete integrations of soundproof and compressible PDEs of atmospheric dynamics. *J. Comput. Phys.*, **263**, 185–205, <https://doi.org/10.1016/j.jcp.2014.01.031>.
- , —, and —, 2019: Semi-implicit integrations of perturbation equations for all-scale atmospheric dynamics. *J. Comput. Phys.*, **376**, 145–159, <https://doi.org/10.1016/j.jcp.2018.09.032>.
- Snively, J. B., and V. P. Pasko, 2008: Excitation of ducted gravity waves in the lower thermosphere by tropospheric sources. *J. Geophys. Res.*, **113**, A06303, <https://doi.org/10.1029/2007JA012693>.
- Suzuki, S., T. Nakamura, M. K. Ejiri, M. Tsutsumi, K. Shiokawa, and T. D. Kawahara, 2010: Simultaneous airglow, lidar, and radar measurements of mesospheric gravity waves over Japan. *J. Geophys. Res.*, **115**, D24113, <https://doi.org/10.1029/2010JD014674>.
- Vadas, S. L., and D. C. Fritts, 2001: Gravity wave radiation and mean responses to local body forces in the atmosphere. *J. Atmos. Sci.*, **58**, 2249–2279, [https://doi.org/10.1175/1520-0469\(2001\)058<2249:GWRAMR>2.0.CO;2](https://doi.org/10.1175/1520-0469(2001)058<2249:GWRAMR>2.0.CO;2).
- , —, and M. J. Alexander, 2003: Mechanism for the generation of secondary waves in wave breaking regions. *J. Atmos. Sci.*, **60**, 194–214, [https://doi.org/10.1175/1520-0469\(2003\)060<0194:MFTGOS>2.0.CO;2](https://doi.org/10.1175/1520-0469(2003)060<0194:MFTGOS>2.0.CO;2).
- Wagner, J., and Coauthors, 2017: Observed versus simulated mountain waves over Scandinavia – Improvement of vertical winds, energy and momentum fluxes by enhanced model resolution? *Atmos. Chem. Phys.*, **17**, 4031–4052, <https://doi.org/10.5194/acp-17-4031-2017>.
- Wirth, V., 2001: Cyclone–anticyclone asymmetry concerning the height of the thermal and the dynamical tropopause. *J. Atmos. Sci.*, **58**, 26–37, [https://doi.org/10.1175/1520-0469\(2001\)058<0026:CAACTH>2.0.CO;2](https://doi.org/10.1175/1520-0469(2001)058<0026:CAACTH>2.0.CO;2).
- Witschas, B., S. Rahm, A. Dörnbrack, J. Wagner, and M. Rapp, 2017: Airborne wind lidar measurements of vertical and horizontal winds for the investigation of orographically induced gravity waves. *J. Atmos. Oceanic Technol.*, **34**, 1371–1386, <https://doi.org/10.1175/JTECH-D-17-0021.1>.
- , S. Gisinger, S. Rahm, A. Dörnbrack, D. C. Fritts, and M. Rapp, 2023: Airborne coherent wind lidar measurements of the momentum flux profile from orographically induced gravity waves. *Atmos. Meas. Tech.*, **16**, 1087–1101, <https://doi.org/10.5194/amt-16-1087-2023>.
- Woods, B. K., and R. B. Smith, 2010: Energy flux and wavelet diagnostics of secondary mountain waves. *J. Atmos. Sci.*, **67**, 3721–3738, <https://doi.org/10.1175/2009JAS3285.1>.
- , and —, 2011: Short-wave signatures of stratospheric mountain wave breaking. *J. Atmos. Sci.*, **68**, 635–656, <https://doi.org/10.1175/2010JAS3634.1>.
- Wurtele, M. G., R. D. Sharman, and A. Datta, 1996: Atmospheric lee waves. *Annu. Rev. Fluid Mech.*, **28**, 429–476, <https://doi.org/10.1146/annurev.fl.28.010196.002241>.
- Zhang, F., J. Wei, M. Zhang, K. P. Bowman, L. L. Pan, E. Atlas, and S. C. Wofsy, 2015: Aircraft measurements of gravity waves in the upper troposphere and lower stratosphere during the START08 field experiment. *Atmos. Chem. Phys.*, **15**, 7667–7684, <https://doi.org/10.5194/acp-15-7667-2015>.